

Resolvent-based estimation of a turbulent wake

Junoh Jung^{*1, 2} and Aaron Towne¹

¹Department of Mechanical Engineering, University of Michigan, Ann Arbor, MI, USA

²Mathematics and Computer Science Division, Argonne National Laboratory, Lemont 60439 IL, USA

Abstract. We present a resolvent-based framework for estimating turbulent velocity fluctuations in the wake of a spanwise-periodic NACA0012 airfoil at Mach 0.3, Reynolds number 23,000, and an angle of attack of 6° . Building on the methodology of Jung *et al.* (*J. Fluid Mech.* 2025, vol. 0, A1), we extend the approach to the more complex regime of a turbulent wake, which involves three primary challenges: (1) globally unstable modes in the linearized Navier–Stokes operator, (2) multi-scale turbulent structures, and (3) high-dimensional datasets. To address these challenges, we employ a data-driven approach that constructs causal resolvent-based estimation kernels from cross-spectral densities obtained via large-eddy simulations. These kernels are derived using the Wiener–Hopf method, which optimally enforces causality, thereby enhancing real-time estimation accuracy. The framework captures the spectral signatures of coherent structures and incorporates the colored statistics of nonlinear forcing terms acting on the linear system. To handle the computational demands of the high-dimensional estimation problem, we utilize parallel algorithms developed within the same framework. We further investigate sensor placement by analyzing single-sensor estimation error and coherence with target flow quantities. Results demonstrate accurate causal estimation of streamwise velocity for the spanwise-averaged, spanwise-Fourier-transformed, and mid-span flow using limited shear-stress measurements on the surface of the airfoil. This study underscores the potential of the resolvent-based framework for efficient estimation in compressible, turbulent environments.

1 Introduction

The estimation of turbulent wakes has been a longstanding focus in fluid mechanics, with decades of experimental and numerical studies revealing their complex dynamics across a range of conditions [Gartshore, 1967, Reynolds, 1972, Ghaemi and Scarano, 2011, Shamsoddin and Porté-Agel, 2017, Gupta *et al.*, 2023, Schauerte and Schreyer, 2024]. At moderate Reynolds numbers (e.g., $Re \approx 20,000$) and mid-range angles of attack ($6^\circ - 10^\circ$), a turbulent wake forms downstream of a laminar separation bubble and exhibits vortex shedding near a characteristic Strouhal number ($St_\alpha \approx 0.2$) based on airfoil thickness [Ducoin *et al.*, 2016, Yeh and Taira, 2019]. Despite the complexity of these flows, even non-physics-based models have successfully estimated key features using experimental data alone [Hoćevan *et al.*, 2005]. These results motivate the development of estimation methods that are not only accurate and interpretable but also suitable for real-time applications.

Among model-based approaches, resolvent analysis has emerged as a powerful tool for studying and

*Email address for correspondence: junohj@umich.edu

estimating turbulent flow structures. By interpreting the linearized Navier–Stokes equations as a forced system, resolvent analysis identifies the input–output relationships associated with the most amplified flow responses in the frequency domain [Jovanović and Bamieh, 2005, McKeon and Sharma, 2010, Towne et al., 2018]. This framework has been used to guide both open-loop and closed-loop control designs. For instance, Yeh and Taira [2019] applied resolvent analysis to identify control parameters for separation control for a NACA airfoil at $Re = 23,000$, $Ma = 0.3$, and angles of attack of 6° and 9° . Similarly, Liu et al. [2021] reduced pressure fluctuations over a cavity using resolvent-informed open-loop control, while Jin et al. [2022] developed a resolvent-based iterative algorithm for closed-loop estimation and control in cylinder flow.

More recently, resolvent-based estimation techniques have shown strong promise in capturing coherent structures in turbulent flows [Towne et al., 2020, Martini et al., 2020, Amaral et al., 2021, Amaral and Cavalieri, 2023, Ying et al., 2023]. These methods leverage the close connection between resolvent modes and spectral proper orthogonal decomposition (SPOD) modes [Towne et al., 2018], enabling data-informed modeling. However, existing implementations have predominantly relied on non-causal formulations, limiting their utility for real-time estimation and control. To address this, recent work developed causal resolvent-based estimators using the Wiener–Hopf formalism [Noble, 1958], which enforces causality [Daniele and Lombardi, 2007, Martinelli, 2009] and yields optimal estimation kernels suited for closed-loop control [Martini et al., 2022] within the incompressible solver Nek5000 [Fischer et al., 2008]. Extending this approach, Jung et al. [2025] developed an efficient computational implementation integrated into the compressible solver CharLES [Brès et al., 2017], successfully validating causal estimation and control methods for a laminar wake flow. Within the same resolvent-CharLES framework, Towne et al. [2024] demonstrated the accuracy of linearized Navier–Stokes operators for various flows, leveraging methods proposed by Nielsen and Kleb [2006] and Bhagwat [2021].

While resolvent analysis is naturally suited to globally stable flows, its extension to globally unstable systems presents challenges. In such cases, the relevance of the resolvent operator becomes less clear, since it is nominally associated with the steady-state response of the system [Colonius and Towne, 2025]. One strategy to mitigate this involves exponential discounting to shift unstable eigenvalues into the stable region of the spectrum [Yeh et al., 2020]. Alternatively, data-driven resolvent formulations have been proposed to bypass the reliance on a globally stable linear operator [Martini et al., 2022, Jung et al., 2025]. These methods maintain the benefits of resolvent-based estimation, specifically by remaining robust against global flow instability.

Sensor placement is crucial for accurate flow estimation, influencing the fidelity of sensor-based measurements and subsequent control strategies. While formal optimization of sensor placement can significantly enhance estimation accuracy [Manohar et al., 2018, Sashittal and Bodony, 2021, Jin et al., 2022], such approaches often face practical limitations due to physical and operational constraints. Consequently, this study does not explicitly aim to optimize realistic sensor placement. Instead, effective sensor locations are determined empirically by assessing coherence between individual sensor–target pairs and by investigating single-sensor estimation errors, thereby providing practical insights relevant to realistic experimental scenarios. Within resolvent-based frameworks, spatial coherence has emerged as a particularly valuable metric for evaluating the suitability of sensor–target pairs. Recent experimental studies [Maia et al., 2021, Audiffred et al., 2023, 2024] and numerical analyses [Towne et al., 2024, Jung et al., 2025] demonstrate that coherence-based approaches effectively identify regions that yield accurate estimation and control. Furthermore, analyzing single-sensor estimation errors offers direct guidance for selecting sensor locations, particularly in high-coherence regions or along predictable disturbance propagation paths [Jung et al., 2025]. Alternatively, streamline visualizations can effectively identify sensor placements dynamically connected to target regions in convectively dominated flows [Jung, 2024].

The objective of the present study is to estimate unsteady turbulent fluctuations in the wake of a NACA 0012 airfoil at $Re = 23,000$ using limited measurements on the surface of the airfoil. Building on our prior work on a laminar wake [Jung et al., 2025], we employ a causal resolvent-based estimation approach

and focus on estimating velocity fluctuations in the turbulent wake, for which the flow exhibits broadband, multi-scale dynamics rather than periodic shedding. Unlike the laminar case, no upstream forcing is required to induce chaotic fluctuations; instead, we estimate naturally occurring turbulent fluctuations. The linearized Navier–Stokes operator in this regime is globally unstable, making traditional resolvent formulations poorly suited. To address this, we adopt a data-driven approach that constructs transfer functions from nonlinear simulation data, using empirical cross-spectral densities to approximate the resolvent operator [Martini et al., 2022, Jung et al., 2025]. These estimators leverage the statistical structure of colored-in-time nonlinear forcing [Towne et al., 2020] and can be constructed without a priori model reduction, maintaining computational efficiency. Furthermore, we enforce causality through a Wiener–Hopf-based formalism [Noble, 1958], enabling real-time estimation for control applications [Jung et al., 2020, Martini et al., 2022]. This work demonstrates that resolvent-based methods can provide accurate, interpretable, and scalable estimators for spanwise-periodic turbulent wakes by exploiting coherent flow structures [Towne et al., 2018].

The remainder of this paper is organized as follows. In §2, we describe the flow configuration, numerical simulations, validation procedures, and the dataset used to construct data-driven estimation kernels, including definitions of three cases: spanwise-averaged, spanwise-Fourier, and mid-span plane. In §3, we briefly outline the resolvent-based estimation framework, including the theoretical formulation, the derivation of the causal resolvent-based estimation kernels via the Wiener-Hopf method, and implementation of the resolvent-based estimation tools. Estimation results for the three cases are discussed in detail in §4. Finally, concluding remarks and future research directions are presented in §5.

2 Problem set-up

2.1 Problem description

We consider the turbulent wake of a NACA0012 airfoil at a moderate chord-based Reynolds number of $Re_{L_c} = 23,000$ and an angle of attack of $\alpha = 6^\circ$, as studied in several previous works [Kojima et al., 2013, Munday and Taira, 2018, Yeh and Taira, 2019, Towne et al., 2023]. The free-stream Mach number is set to $M_\infty \equiv u_\infty/c_\infty = 0.3$, where u_∞ and c_∞ denote the free-stream velocity and sound speed, respectively. Shear-stress sensors are placed on the airfoil surface, while the targets are located downstream in the turbulent wake (see §4 for details). In this paper, we present a resolvent-based estimation of the time-series fluctuations in the streamwise velocity u'_x around the mean flow \bar{u}_x .

2.2 Simulation

A large-eddy simulation (LES) utilizing the high-fidelity compressible flow solver CharLES from Cadence Design Systems [Brès et al., 2017, 2018, Yeh and Taira, 2019, Brès et al., 2022] is conducted to simulate turbulent airfoil flow. The simulation is conducted on Koehr, the Department of Defense’s supercomputer, an HPE SGI 8600 system with a peak performance of 3.05 PFLOPS. For this study, 50 nodes of the supercomputer, each equipped with 48 cores, were utilized. A C-shaped mesh, generated using Pointwise, is depicted in figure 1(a). Figures 1(b) and (c) illustrate the mean, instantaneous streamwise velocity field, respectively. The airfoil’s leading edge is positioned at the origin, $x/L_c = y/L_c = 0$. The computational domain spans $x/L_c \in [-20, 21]$, $y/L_c \in [-20, 20]$, and $z/L_c \in [-0.1, 0.1]$. To optimize the mesh resolution, adaptive refinement was employed in the transverse and spanwise directions. A characteristic boundary condition $[\rho, u_x, u_y, u_z, P] = [\rho_\infty, U_\infty, 0, 0, P_\infty]$ was applied at the domain edges, with a sponge layer implemented for $x/L_c \in [11, 21]$ to mitigate spurious reflections at the outflow. The time integration used a constant Courant-Friedrichs-Lewy (CFL) number of 0.84.

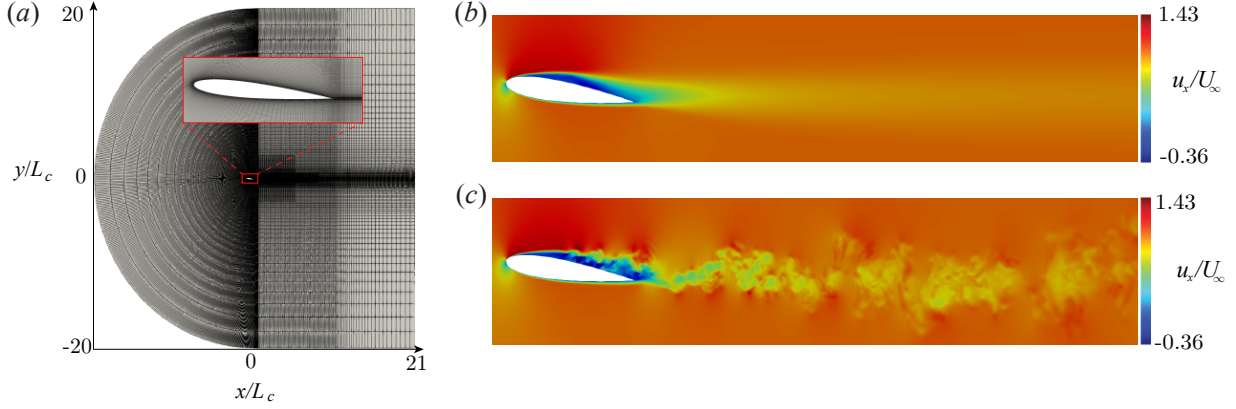


FIGURE 1: Computational mesh and simulation: (a) the complete C-shaped grid, with a zoomed-in view of the mesh near the wall shown in the inset; (b) the mean streamwise velocity u_x ; and (c) a snapshot of the instantaneous streamwise velocity u_x obtained from the large-eddy simulation.

	\bar{C}_D	\bar{C}_L
Present study	0.0663	0.5836
Yeh and Taira [2019]	0.066	0.609
Munday and Taira [2018]	0.062	0.637
Kojima et al. [2013]	0.054	0.639

TABLE 1: Comparison of the time-averaged drag and lift coefficients with the reference data for a NACA 0012 airfoil at $Re_{L_c} = 23,000$ and angle of attack 6° .

We validate the LES by comparing the pressure coefficient and aerodynamic forces

$$C_p = \frac{p - p_\infty}{\frac{1}{2}\rho_\infty U_\infty^2}, \quad C_D = \frac{F_D}{\frac{1}{2}\rho_\infty U_\infty^2 A}, \quad \text{and} \quad C_L = \frac{F_L}{\frac{1}{2}\rho_\infty U_\infty^2 A} \quad (2.1)$$

with previous works in table 1 and figure 2. Experimental data is provided by Kim et al. [2009]. The closest analogue to our simulation is that of Yeh and Taira [2019], which entails the same physical setup and solver but a different grid. The simulations of Kojima et al. [2013] and Munday and Taira [2018] differ due to their use of an incompressible flow solver.

As shown in figure 3, the shear layer roll-up on the suction surface occurs at $x/L_c \approx 0.4$, leading to spanwise vortices. A laminar separation bubble is observed on the suction side of the airfoil in the region $0.1 \lesssim x/L_c \lesssim 0.84$, as indicated by the mean streamwise velocity shown in figure 1(b). Laminar-turbulent transition is detected at $x/L_c \approx 0.6$, as determined by the termination of the pressure coefficient plateau illustrated in figure 2. Finally, a turbulent wake develops behind the airfoil.

2.3 Dataset

We consider three distinct representations of the spanwise-periodic flow: spanwise-averaged, spanwise-Fourier, and mid-span plane cases. The spanwise-averaged case is the simplest representation, defined mathematically as

$$\mathbf{q}_{\text{span-avg}}(x, y, t) = \frac{1}{L_z} \int_0^{L_z} \mathbf{q}(x, y, z, t) dz, \quad (2.2)$$

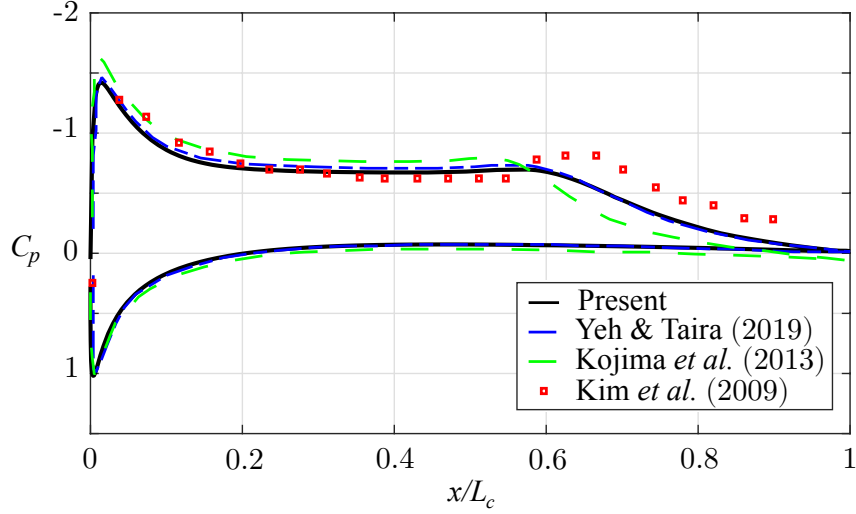


FIGURE 2: Comparison of the pressure coefficient C_p with previous works.

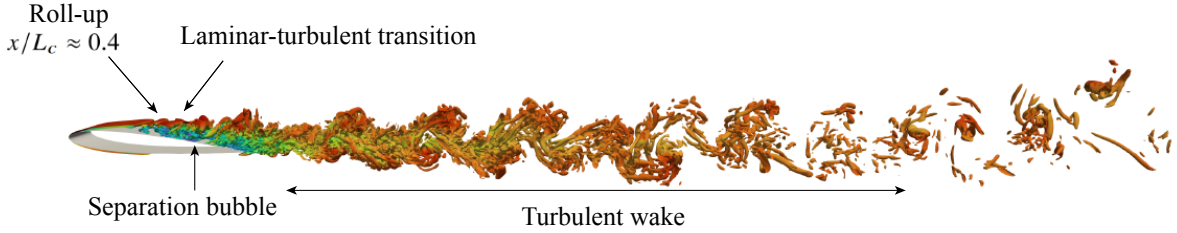


FIGURE 3: Q-criterion visualization showing the key flow features.

where L_z is the spanwise length. Spanwise-Fourier decomposition, a common technique in biglobal stability analyses of three-dimensional flows [Theofilis, 2003], has been previously utilized to investigate resolvent gains at various spanwise wavenumbers [Yeh and Taira, 2019, Towne et al., 2023]. We similarly analyze spanwise-Fourier modes defined by

$$\hat{\mathbf{q}}(x, y, k_z, t) = \frac{1}{L_z} \int_0^{L_z} \mathbf{q}(x, y, z, t) e^{-ik_z z} dz, \quad (2.3)$$

where k_z denotes the spanwise wavenumber. This approach allows us to progressively incorporate more complex flow structures by examining the spanwise Fourier modes. Finally, the mid-span plane case focuses on the flow at the central spanwise location, defined as

$$\mathbf{q}_{\text{mid}}(x, y, t) = \mathbf{q}(x, y, z_{\text{mid}}, t), \quad (2.4)$$

where $z_{\text{mid}} = L_z/2$ is the mid-span location. This representation helps capture spanwise effects in the estimation process by examining the flow at a representative spanwise position and is consistent with a realistic use case where sensors are distributed along the airfoil at a single spanwise position. These representations enhance our understanding of spanwise effects in the flow and support investigations into sensor placement

and flow estimation strategies for a spanwise-periodic flow.

The dataset comprises $n_t = 75,000$ time-resolved, three-dimensional snapshots of $[\rho, \rho u_x, \rho u_y, \rho u_z, T]$, spanning a nondimensional time window of $tU_\infty/L_c \in [0, 324]$. These snapshots are sampled at a uniform interval of $\Delta t U_\infty/L_c = 0.00432$, which resolves the dominant vortex-shedding frequency at $St_\alpha \equiv fL_c(\sin\alpha)/U_\infty \approx 0.15$. This finer temporal resolution and longer duration compared to previous datasets [Towne et al., 2023] enable capturing smaller-scale turbulent fluctuations in time and provide a larger number of snapshots, resulting in improved convergence of the estimation kernels. The time window captures approximately 466 shedding cycles, providing a sufficiently long time series to ensure statistical convergence of spectral quantities, including the cross-spectral densities used in constructing the estimation kernel. The spatial domain covers $x/L_c \in [-0.5, 2.5]$ and $y/L_c \in [-0.5, 0.5]$, capturing the near-wake region with high spatial fidelity.

To construct resolvent-based estimation kernels, we follow the implementation of Jung et al. [2025]. Prior to estimation, the dataset was preprocessed by subtracting the temporal mean from each variable and applying a Hamming window [Hamming, 1997] to reduce spectral leakage in the Fourier transform. For assessing generalization performance, 80% of the data is used to train the estimation model, while the remaining 20% is reserved for testing.

3 Resolvent-based estimation framework

In this section, we briefly review the resolvent-based estimation framework developed in recent studies [Towne et al., 2020, Martini et al., 2020, 2022, Jung et al., 2025].

3.1 Estimation system

We start with the compressible Navier-Stokes equations written as

$$\frac{\partial \mathbf{q}}{\partial t} = \mathcal{F}(\mathbf{q}), \quad (3.1)$$

where \mathbf{q} is a state vector of flow variables $[\rho, \rho u_x, \rho u_y, \rho u_z, \rho E]^T$ and \mathcal{F} is the nonlinear Navier-Stokes operator. The equations are linearized using a Reynolds decomposition, giving

$$\frac{\partial \mathbf{q}'}{\partial t} - \mathbf{A} \mathbf{q}' = \mathbf{f}(\bar{\mathbf{q}}, \mathbf{q}'), \quad (3.2)$$

where $\bar{\mathbf{q}}$ and \mathbf{q}' represent the mean and perturbation state vectors of the flow variables, respectively, $\mathbf{A} = \frac{\partial \mathcal{F}}{\partial \mathbf{q}}|_{\bar{\mathbf{q}}}$ is the linearized Navier-Stokes operator, and \mathbf{f} represents the remaining nonlinear terms. For convenience, we drop the $(\cdot)'$ superscript for perturbations from this point on.

To derive the estimation method, we consider a generalization of (3.1) in the form of the linear-time-invariant (LTI) system

$$\frac{d\mathbf{q}}{dt}(t) = \mathbf{A}\mathbf{q}(t) + \mathbf{B}_f \mathbf{f}(t), \quad (3.3a)$$

$$\mathbf{y}(t) = \mathbf{C}_y \mathbf{q}(t) + \mathbf{n}(t), \quad (3.3b)$$

$$\mathbf{z}(t) = \mathbf{C}_z \mathbf{q}(t), \quad (3.3c)$$

where the forcing matrix $\mathbf{B}_f \in \mathbb{C}^{n \times n_f}$ can be used to restrict the form of the forcing \mathbf{f} , and the measurement \mathbf{y} and target \mathbf{z} indicate readings of the state perturbation extracted by a measurement matrix $\mathbf{C}_y \in \mathbb{C}^{n_y \times n}$ and

a target matrix $\mathbf{C}_z \in \mathbb{C}^{n_z \times n}$. The number of sensors and targets is denoted n_y and n_z , respectively. The vector \mathbf{n} indicates the sensor noise. The measurement \mathbf{y} is chosen to be the shear stress τ_w at one or more points on the surface of the airfoil. It is computed from the state \mathbf{q} using a suitably defined measurement matrix \mathbf{C}_y , as in Jung et al. [2025]. In line with recent applications of the resolvent-based framework [Amaral et al., 2021, Towne et al., 2024], preliminary tests indicated minimal difference between using shear stress and pressure as the measured quantity on the airfoil surface. The target \mathbf{z} represents one or more Gaussian sensors, each with spatial support given by

$$\alpha e^{-(x-x_c)^2/2\sigma_x^2 - (y-y_c)^2/2\sigma_y^2 - (z-z_c)^2/2\sigma_z^2}, \quad (3.4)$$

where σ_x , σ_y , and σ_z define the width of the Gaussian distribution in each coordinate direction, and α is a weighting factor representing the integrated contribution over the Gaussian support. These targets are extracted from the state using the measurement matrix \mathbf{C}_z .

By Fourier-transforming the linear system into the frequency domain and defining the resolvent operator as $\mathbf{R} = (i\omega\mathbf{I} - \mathbf{A})^{-1}$, where \mathbf{I} is the identity matrix and ω is the frequency, we derive modified resolvent operators used for constructing the resolvent-based kernels for estimation. The measurement and target vectors can be written as

$$\hat{\mathbf{y}} = \mathbf{R}_{yf} \hat{\mathbf{f}} + \hat{\mathbf{n}}, \quad (3.5a)$$

$$\hat{\mathbf{z}} = \mathbf{R}_{zf} \hat{\mathbf{f}} \quad (3.5b)$$

with $\mathbf{R}_{yf} = \mathbf{C}_y \mathbf{R} \mathbf{B}_f$, and $\mathbf{R}_{zf} = \mathbf{C}_z \mathbf{R} \mathbf{B}_f$. The notation $(\hat{\cdot})$ indicates a quantity in the frequency domain.

3.2 Kernels for resolvent-based estimation

We perform estimation with three different kernels: non-causal, truncated non-causal, and causal [Martini et al., 2022]. First, we start with a non-causal estimator using a convolution function, written as

$$\tilde{\mathbf{z}}_{nc}(t) = \int_{-\infty}^{\infty} \mathbf{T}_{nc}(t - \tau) \mathbf{y}_n(\tau) d\tau, \quad (3.6)$$

where $\mathbf{T}_{nc} \in \mathbb{R}^{n_z \times n_y}$ is a non-causal estimation kernel between the sensor measurement and the estimated target state. The objective is to select the kernel to minimize the expected value of the estimation error $e(t) = \tilde{\mathbf{z}} - \mathbf{z}(t)$, and this is formalized by defining the cost function

$$\mathbf{J}_{nc}(t) = \int_{-\infty}^{\infty} \mathbb{E}\{e(t)^\dagger e(t)\} dt, \quad (3.7)$$

where $\mathbb{E}\{\cdot\}$ is the expectation operator. The overall goal can be explained more easily using the block diagram in figure 4(a).

By minimizing the cost function, we obtain a non-causal estimation kernel

$$\hat{\mathbf{T}}_{nc}(\omega) = (\mathbf{R}_{zf} \hat{\mathbf{F}} \mathbf{R}_{yf}^\dagger) (\mathbf{R}_{yf} \hat{\mathbf{F}} \mathbf{R}_{yf}^\dagger + \hat{\mathbf{N}})^{-1}, \quad (3.8)$$

where $\hat{\mathbf{F}} = \mathbb{E}\{\hat{\mathbf{f}} \hat{\mathbf{f}}^\dagger\}$ and $\hat{\mathbf{N}} = \mathbb{E}\{\hat{\mathbf{n}} \hat{\mathbf{n}}^\dagger\}$ denote the forcing and sensor noise cross-spectral density matrices, respectively. Note that the space-time color of the forcing terms is explicitly included in (3.8), which means that the nonlinearity of the flow can be statistically accounted for in the transfer function.

Second, for real-time estimation, the only current and past (but not future) sensor measurements are available to the estimator. One common approach to addressing this practical limitation is to truncate the

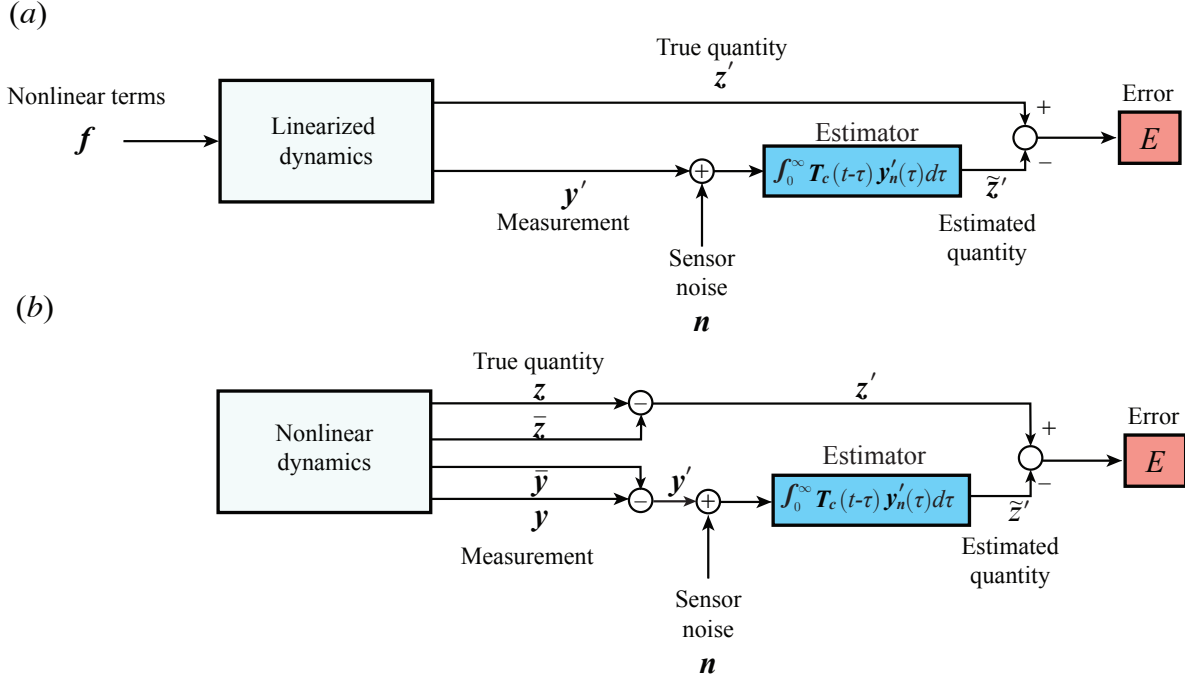


FIGURE 4: Block diagram of resolvent-based estimation: (a) design of the resolvent-based estimator based on the linear system and (b) application to the nonlinear system. Here, $(\cdot)'$ indicates fluctuations around the mean quantity, $(\bar{\cdot})$ denotes mean quantity, and $(\tilde{\cdot})$ represents an estimated quantity.

non-causal kernel by setting the part associated with unavailable future measurements to zero. The truncated non-causal kernel is defined as

$$\mathbf{T}_{inc}(\tau) = \begin{cases} \mathbf{T}_{nc}(\tau), & \tau \geq 0, \\ 0, & \tau < 0. \end{cases} \quad (3.9)$$

The truncated non-causal estimates are computed as

$$\tilde{z}_{inc}(t) = \int_{-\infty}^0 \mathbf{T}_{inc}(t-\tau) y_n(\tau) d\tau. \quad (3.10)$$

Lastly, by enforcing causality via Wiener-Hopf formalism in cost functions, we derive optimal causal estimation kernels under the constraint of causality. A causal estimator

$$\tilde{z}_c(t) = \int_{-\infty}^0 \mathbf{T}_c(t-\tau) y_n(\tau) d\tau, \quad (3.11)$$

is defined in terms of the causal estimation kernel $\mathbf{T}_c \in \mathbb{R}^{n_z \times n_y}$. To enforce causality, we modify the cost function of (3.7) to read

$$\mathbf{J}_c(t) = \int_{-\infty}^{\infty} \mathbb{E}\{e(t)^* e(t)\} + (\mathbf{A}_-(t) \mathbf{T}_c(t) + \mathbf{A}_-^\dagger(t) \mathbf{T}_c^\dagger(t)) dt, \quad (3.12)$$

where \mathbf{A} is a Lagrange multiplier that is used to force the causal kernel to be zero for the non-causal part ($\tau < 0$). The $(\cdot)_+$ and $(\cdot)_-$ subscripts represent the non-causal ($\tau < 0$) and causal ($\tau > 0$) parts of any matrix

or function to be zero by achieving a Wiener-Hopf factorization. Additionally, $[\cdot]_+$ and $(\cdot)_+$ denote additive and multiplicative factorization operators, respectively (see Appendix A for further details). The derived causal kernel for the estimation is

$$\hat{\mathbf{T}}_c(\omega) = [\mathbf{R}_{zf} \hat{\mathbf{F}} \mathbf{R}_{yf}^\dagger (\mathbf{R}_{yf} \hat{\mathbf{F}} \mathbf{R}_{yf}^\dagger + \hat{\mathbf{N}})^{-1}]_+ (\mathbf{R}_{yf} \hat{\mathbf{F}} \mathbf{R}_{yf}^\dagger + \hat{\mathbf{N}})^{-1}. \quad (3.13)$$

All the transfer functions we consider involve the forcing cross-spectra density matrix that can account for the impact of the nonlinearity in a statistical sense. However, our method is more suitable for the real-time estimation approach since causality is constrained. In this paper, we present the results for both the causal and truncated non-causal transfer functions to assess how optimally enforcing causality impacts the estimation accuracy for turbulent flow.

The resolvent operators appearing in the estimation kernels are not well-defined for globally unstable systems [Jovanović and Bamieh, 2005, Yeh et al., 2020] such as the linearization of the turbulent airfoil wake about its mean [Yeh and Taira, 2019]. To circumvent this issue, we use a data-driven approach [Martini et al., 2022] that enables the construction of resolvent-based kernels without the need to explicitly form resolvent operators. The empirical cross-spectra densities (CSD) from the simulation are used to obtain the modified resolvent operators, which is a similar way to the previous work [Audiffred et al., 2023, Jung et al., 2025]. Following the notation of the LTI system in §3.1, the datasets of the sensor and target readings are Fourier-transformed, expressed as

$$\begin{bmatrix} \hat{\mathbf{y}} \\ \hat{\mathbf{z}} \end{bmatrix} = \begin{bmatrix} \mathbf{R}_{y,f} & 1 \\ \mathbf{R}_{z,f} & 0 \end{bmatrix} \begin{bmatrix} \hat{\mathbf{f}} \\ \hat{\mathbf{n}} \end{bmatrix}. \quad (3.14)$$

Computing the cross-spectral density of $[\hat{\mathbf{y}} \quad \hat{\mathbf{z}}]^T$ gives

$$\begin{bmatrix} \mathbf{S}_{yf,yf} & \mathbf{S}_{yf,zf} \\ \mathbf{S}_{zf,yf} & \mathbf{S}_{zf,zf} \end{bmatrix} = \begin{bmatrix} \mathbf{R}_{yf} \hat{\mathbf{F}} \mathbf{R}_{yf}^\dagger & \mathbf{R}_{yf} \hat{\mathbf{F}} \mathbf{R}_{zf}^\dagger \\ \mathbf{R}_{zf} \hat{\mathbf{F}} \mathbf{R}_{yf}^\dagger & \mathbf{R}_{zf} \hat{\mathbf{F}} \mathbf{R}_{zf}^\dagger \end{bmatrix}, \quad (3.15)$$

with $\mathbf{S}_{yf,yf} = \mathbb{E}\{\hat{\mathbf{y}}\hat{\mathbf{y}}^*\}$ and $\mathbf{S}_{zf,yf} = \mathbb{E}\{\hat{\mathbf{z}}\hat{\mathbf{y}}^*\}$. Since the right-hand side of (3.15) contains the terms needed to build the estimation kernels, this shows that the correlations on the left-hand side can be used in their place in (3.8) and (3.13). The data-driven non-causal and causal estimation kernels in (3.8) and (3.13) are computed using the CSDs from (3.15), yielding

$$\hat{\mathbf{T}}_{nc} = \mathbf{S}_{zy} (\mathbf{S}_{yy} + \hat{\mathbf{N}})^{-1}, \quad (3.16a)$$

$$\hat{\mathbf{T}}_c = [\mathbf{S}_{zy} (\mathbf{S}_{yy} + \hat{\mathbf{N}})^{-1}]_+ (\mathbf{S}_{yy} + \hat{\mathbf{N}})^{-1}. \quad (3.16b)$$

Note that the CSDs inherently contain statistical information related to the nonlinearities of the flow within the forcing covariance matrix. The mean flow is subtracted from both the measurement readings and target values. Estimation kernels are computed offline for the linear system, as illustrated in figure 4(a). These kernels are then used for real-time (online) estimation of velocity fluctuations in the wake, applying the approach to the nonlinear system, as depicted in figure 4(b).

3.3 Implementation of resolvent-based estimation

We employ recently developed resolvent-based estimation and control tools integrated within the compressible flow solver CharLES [Jung et al., 2024, Towne et al., 2024], which was carefully designed to scale to large-scale problems such as a turbulent wake. Originally inspired by the incompressible solver implementation by Martini et al. [2022], the approach was extended by Jung et al. [2025] to compressible flows using parallel algorithms written in C++, built directly upon the existing solver architecture. These resolvent-based

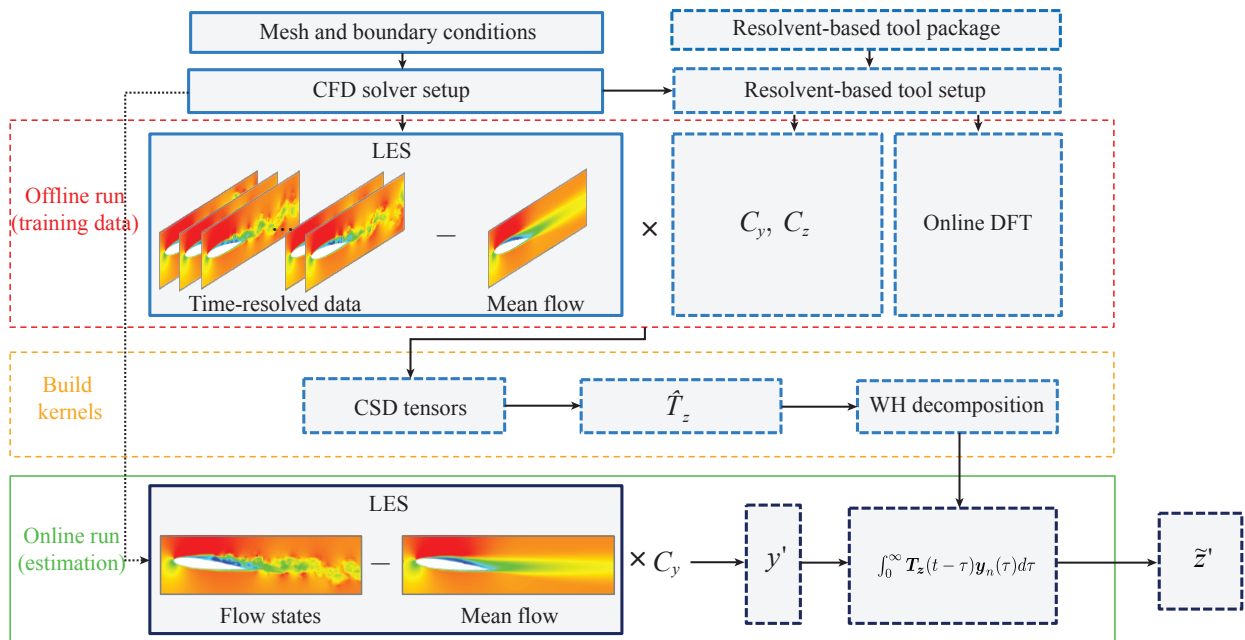


FIGURE 5: Flowchart of the resolvent-based estimation tool within a compressible flow solver. Dashed-line boxes represent the resolvent-based tool integrated into the existing CFD solver (solid-line box). Blue boxes, including those outlined in red (offline run) and orange (build kernels) dashed lines, indicate offline processes, while black boxes with green solid outlines represent online (estimation) processes.

tools interact with the solver, enabling efficient in-situ computations during simulations. Moreover, our modular software design simplifies integration with other relevant software packages and ensures straightforward deployment in high-performance computing environments.

An overview of the implementation is shown in figure 5. Our compressible resolvent-based tool integrates external libraries such as PETSc [Balay et al., 2019] and FFTW [Frigo and Johnson, 2005], enabling scalable parallel computation through in-situ matrix operations with flow quantities during the training process. The tool constructs measurement matrices (C_y and C_z) using control volume indices from the CFD mesh. For cases involving high-rank targets ($n_z \gg n_y$), an online discrete Fourier transform (DFT) is used to minimize memory consumption while preserving time-resolved information [Schmidt and Towne, 2019, Farghadan et al., 2024, 2025]. Training data is obtained from large eddy simulations (LES), and the corresponding cross-spectral densities (CSDs) are used to generate the estimation kernels. The DFT parameters used to obtain converged kernels are described in Appendix B.

4 Results

We demonstrate the effectiveness of the causal resolvent-based approach for predicting turbulent fluctuations over a NACA0012 airfoil at a 6° angle of attack. Unlike earlier resolvent-based studies that employed non-causal estimation methods [Towne et al., 2020, Martini et al., 2020, Amaral et al., 2021, Amaral and Cavalieri, 2023], the causal estimator uses only present and past measurements and kernels optimized for this purpose via the Wiener-Hopf method [Martini et al., 2022]. This causality enforcement makes our method particularly suitable for real-time applications. Significantly, this work is the first numerical investigation

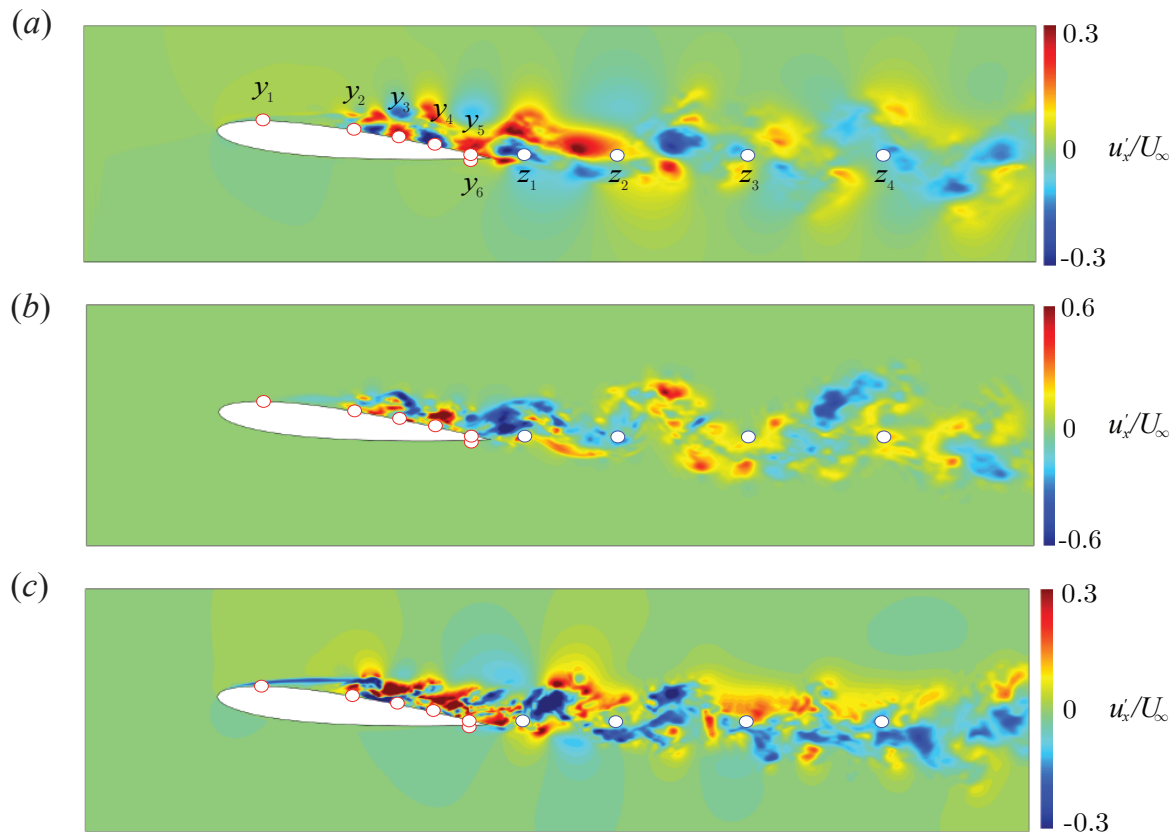


FIGURE 6: Streamwise velocity fluctuation fields (u'_x/U_∞) for (a) spanwise-average, (b) spanwise-Fourier mode $k_z = 10\pi$, and (c) mid-span plane case. Target locations (z_1, z_2, z_3, z_4) are indicated by blue circles and positioned along the trailing edge at streamwise coordinates $x/L_c = [1.2, 1.5, 2.0, 2.5]$ for a constant transverse position $y/L_c = -0.11$.

explicitly applying the Wiener-Hopf method to enforce causality in turbulent flow estimation [Jung and Towne, 2024], extending previous efforts primarily focused on experimental flow-control studies [Audiffred et al., 2023, 2024] and laminar-flow scenarios [Martini et al., 2022, Jung et al., 2025].

As previously mentioned, our analysis centers on the spanwise-averaged, spanwise-Fourier, and mid-span plane cases, as depicted in figure 6. The specific target locations analyzed in the wake region are also highlighted in figure 6(a). The spanwise-averaged case provides a concise yet informative view of spatial structure in the spanwise direction, enabling a focused analysis of sensor positioning in the streamwise and cross-stream planes. We progressively incorporate more complex flow structures by examining the spanwise-Fourier modes, with particular attention to the most energetic mode at $k_z = 10\pi$, and the flow on the mid-span plane to better capture spanwise effects in the estimation process.

Given the large number of potential sensor positions available on the three-dimensional airfoil surface, our investigation begins with selecting the most effective sensor locations based on single-sensor estimation error metrics and coherence analyses. Subsequently, we examine the power spectral density (PSD) at these selected sensor and target locations to better understand their frequency-domain characteristics. We then construct estimation kernels specifically designed for multi-sensor estimation, analyzing their characteristics in both the time and frequency domains to gain insight into their role in estimation performance. Finally, we present multi-sensor estimation results, quantifying errors at both single target points and over extended

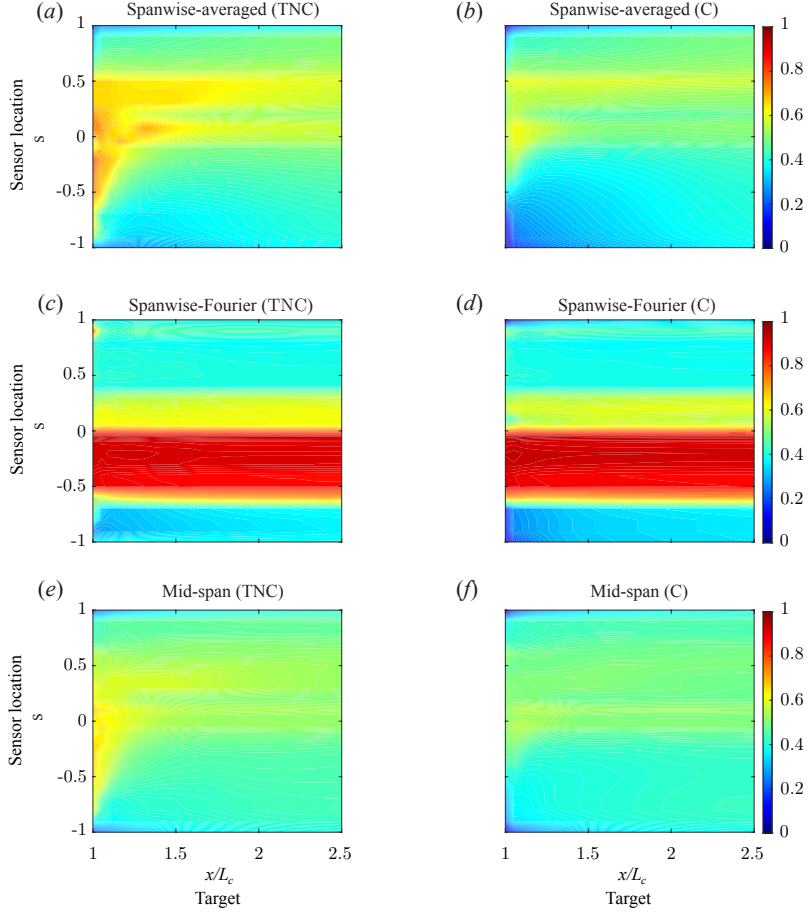


FIGURE 7: Estimation error maps for the streamwise velocity fluctuation u'_x in single sensor-target configurations: (a, b) spanwise-averaged flow, (c, d) spanwise-Fourier mode for $k_z = 10\pi$, and (e, f) mid-span plane flow. Results using the truncated non-causal approach are shown in panels (a, c, e), while the causal estimation results are shown in panels (b, d, f).

target regions, to demonstrate the accuracy of the resolvent-based method.

4.1 Investigation of sensor placement

Sensor placement is guided by evaluating single-sensor estimation error metrics, similar to the approach in Jung et al. [2025], as well as assessing coherence between sensor and target locations [Maia et al., 2021, Audiffred et al., 2024]. The estimation error used throughout this paper is quantified by the metric [Martini et al., 2022, Jung and Towne, 2024, Jung et al., 2025]

$$E = \frac{\sum_i \int (\tilde{z}_i(t) - z_i(t))^2 dt}{\sum_i \int (z_i(t))^2 dt}, \quad (4.1)$$

where \tilde{z}_i and z_i represent the estimated and true values at the i -th target location, respectively. Additionally, coherence provides valuable insights into frequency-dependent estimation performance and is defined as

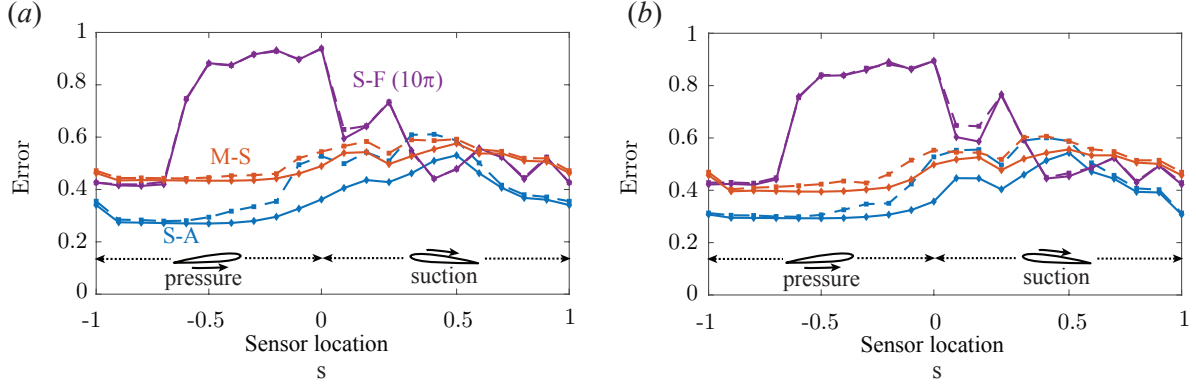


FIGURE 8: Estimation errors of streamwise (a) and cross-streamwise (b) velocities as a function of the sensor location on the airfoil surface. The blue, orange, purple, and green lines represent spanwise-averaged (S-A), mid-span (M-S), and spanwise-Fourier (S-F) ($K_z = 10\pi$) flows, respectively. The solid diamond (\diamond) and dashed square (\square) lines denote the causal and truncated non-causal approaches, respectively.

[Towne et al., 2020]:

$$\hat{\gamma}_{yz}(\omega) = \frac{|\hat{\mathbf{S}}_{yz}(\omega)|}{\sqrt{\hat{\mathbf{S}}_{yy}(\omega)}\sqrt{\hat{\mathbf{S}}_{zz}(\omega)}}, \quad (4.2)$$

where $\hat{\mathbf{S}}_{yz}$ denotes the cross-spectral density between sensor and target, and $\hat{\mathbf{S}}_{yy}$ and $\hat{\mathbf{S}}_{zz}$ denote their respective power spectral densities.

Figure 7 presents spatial maps of estimation errors for a single sensor estimating streamwise velocity fluctuations at a single target location. Results are compared between the truncated non-causal (panels a, c, e) and causal (panels b, d, f) estimation approaches, covering three different flow representations: spanwise-averaged case (panels a, b), spanwise-Fourier modes at wavenumbers $k_z = 10\pi$ (panel c, d), and mid-span plane case (panels e, f). For the spanwise-Fourier case, we focus specifically on the wavenumber $k_z = 10\pi$, as it represents the lowest frequency and highest energy modes identified by previous resolvent gain studies [Yeh and Taira, 2019, Towne et al., 2023].

Sensor locations are characterized using the coordinate s , defined such that positive values correspond to the suction surface and negative values to the pressure surface of the airfoil, with the magnitude representing the normalized streamwise position (x/L_c). Overall, the causal estimation method consistently outperforms the truncated non-causal approach. This advantage is particularly noticeable near the trailing-edge region ($1 < x/L_c < 1.5$) and prominently so when sensors are positioned on the front surfaces of the airfoil ($-0.5 < s < 0.5$). The performance improvement is more pronounced for the spanwise-averaged flow compared to the mid-span flow. This difference arises primarily due to the characteristics of the laminar region spanning $-0.5 < s < 0.5$ on the surface of the airfoil, where larger spanwise structures exist, resulting in less information about turbulent fluctuations in the wake, diminishing estimation accuracy. The detrimental impact of laminar regions on estimation accuracy is especially evident in the spanwise Fourier modes. For the spanwise Fourier modes, sensors located within the laminar region ($-0.5 < s < 0.5$), particularly on the pressure surface ($-0.5 < s < 0$), exhibit poor estimation performance. This effect is notably stronger at low wavenumbers, e.g., $k_z = 10\pi$, likely due to its larger associated spanwise structures compared to higher wavenumbers, e.g., $k_z = 20\pi$. However, downstream of the laminar-to-turbulent transition, estimation performance significantly improves due to the emergence of large-scale turbulent structures within the wake that are better correlated with the measurements.

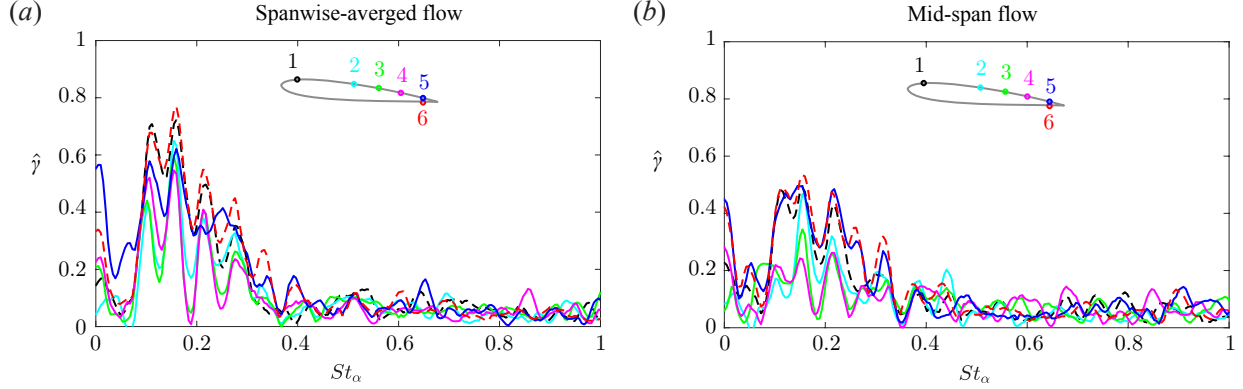


FIGURE 9: Coherence of the streamwise velocity with respect to the target $z_1(x/L_c = 1.2)$ for the spanwise-averaged and mid-span flows.

Figure 8 presents the average estimation errors over the wake region as a function of sensor location s , comparing spanwise-averaged (S-A), spanwise-Fourier (S-F), and mid-span plane (M-S) flows. These results are shown separately for the streamwise velocity fluctuations (u'_x , panel *a*) and the cross-streamwise velocity fluctuations (u'_y , panel *b*). Here, we report the average error over a set of targets in the wake that are uniformly distributed along the line segment $1 < x/L_c < 2.5$ and $y/L_c = -0.11$. The resolvent-based kernels, which inherently include the linearized Navier–Stokes operator, effectively estimate both velocity components from shear-stress sensor measurements. This effectiveness implies potential applicability of our method for estimating other relevant flow quantities, such as the vorticity field. Sensors placed on the pressure surface generally yield higher accuracy in spanwise-averaged and mid-span flows. Interestingly, the laminar region on the suction surface also performs well for estimation in spanwise-averaged flows, which contrasts with the results shown previously in figure 7. This discrepancy arises because the targets analyzed in figure 8 span both the upper and lower wake regions relative to the trailing edge, thereby incorporating regions of different coherence characteristics. Additionally, we observe a slight deterioration in estimation accuracy for sensors within the laminar separation bubble region ($0.4 < s < 0.7$), although accuracy improves progressively as the sensor location approaches the trailing edge. Overall, superior estimation performance is achieved for the spanwise-averaged flow compared to the mid-span flow, with the spanwise Fourier modes exhibiting intermediate performance. Based on these observations, sensor positions near the trailing edge ($0.5 < x < 1$) and on the upstream suction ($0 < x < 0.3$) and pressure ($-1 < x < -0.7$) surfaces are identified as particularly effective locations for achieving high-performance resolvent-based estimation.

In figure 9, we examine coherence of the streamwise velocity fluctuations between the sensor and the wake regions for the spanwise-averaged and mid-span flows at the sensor locations where single-sensor estimation was effective, as demonstrated in figures 7 and 8. These locations include regions on the front suction side ($0 < x/L_c < 0.3$), the rear pressure side ($-1 < x/L_c < -0.7$), and the mid-chord area ($0.5 < x/L_c < 1$), as illustrated in figures 9. Since our goal in this coherence study is to gain physical insights into coherence between sensor locations and wake fluctuations, we focus our analysis on the near-wake target position at $x/L_c = 1.2$. We confirmed that coherence trends at farther wake positions were similar but with reduced magnitudes. Specifically, the sensors representing the laminar regions were placed at 1 (suction side, laminar region $0 < x/L_c < 0.4$) and 6 (pressure side, laminar region $-1 < x/L_c < 0$), as shown in figure 9. Within each laminar region, the coherence patterns remain similar, differing only in magnitude. Notably, spanwise-averaged flow fields exhibit stronger coherence at frequencies of interest ($St_\alpha < 0.2$) compared to mid-span flows. This enhanced coherence results from spatially larger coherent fluctuations associated

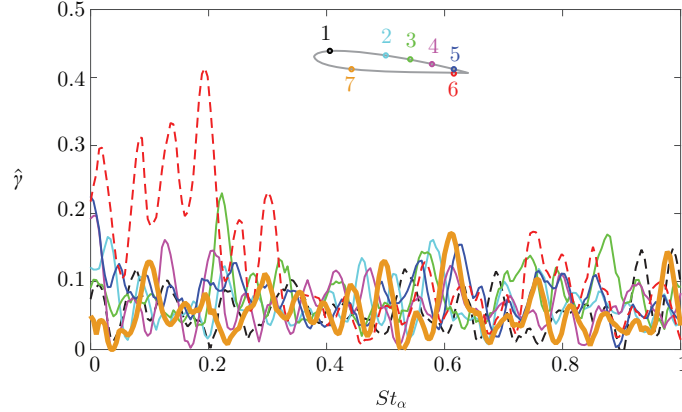


FIGURE 10: Coherence of the streamwise velocity with respect to the target $z_1 (x/L_c = 1.2)$ of the spanwise-Fourier case at $k_z = 10\pi$.

with spanwise averaging, resulting in stronger coupling between sensor and target fluctuations. Interestingly, laminar regions (sensors 1 and 6) exhibit significant coherence with the near-wake target, suggesting that upstream laminar disturbances may be inherently linked to downstream wake fluctuations [Jung et al., 2025]. Furthermore, sensor 5, located in the turbulent region, demonstrates notable coherence with the target across a wide frequency range. Among middle locations (sensors 2, 3, and 4), each sensor displays pronounced coherence at the frequency bands of interest ($St_\alpha < 0.2$). These locations are empirically selected to capture dominant frequencies at the target, which are crucial for kernel-based amplification in the frequency domain.

We further investigated coherence between the sensor and the wake regions with respect to the streamwise velocity fluctuations for the spanwise-Fourier mode at $k_z = 10\pi$. In particular, we are interested in verifying whether coherence is indeed weak in the region $-0.7 < x/L_c < 0$, as shown in the single-sensor estimation result in figure 7. To assess this, we examined coherence at sensor location 7, placed at $x/L_c = -0.3$, as indicated by the yellow solid line in figure 10. Although the von Kármán vortex shedding and other dominant frequencies are evident for $St_\alpha < 0.2$, sensor 7 does not exhibit significant coherence in this frequency range. In contrast, sensor locations 4 (purple), 5 (blue), and 6 (red) display prominent coherence peaks, consistent with effective estimation performance. Figure 10 further indicates that sensors 5 and 6 exhibit increased coherence at a spanwise frequency of 10π . Ultimately, we identify sensors 1, 5, and 6 as the most effective for estimation purposes, with an additional selection of sensor 4 from among sensors 2, 3, and 4.

4.2 Power-spectral density of the sensor and target readings

Figure 11 presents the power spectral density (PSD) of the sensor and target signals for the spanwise-averaged, spanwise-Fourier, and mid-span plane flows. Panels (a) and (b) highlight three dominant frequencies evident in the signals at sensor positions y_3 , y_4 , and y_5 , as well as the target position z_1 . The energy associated with these dominant frequencies decreases downstream, as demonstrated by the PSD at target positions z_2 , z_3 , and z_4 in panel (b). It is well established that laminar separation bubble (LSB) detachment over the suction surface promotes the Kelvin–Helmholtz instability, resulting in vortex shedding characterized by lower-frequency oscillations ($St_\alpha < 0.12$) [Ducoin et al., 2016]. These lower-frequency peaks are clearly captured in panel (a) for sensor positions y_3 , y_4 , y_5 , and the near-wake target z_1 . In contrast, the turbulent region on the airfoil surface and near wake exhibit dominant von Kármán vortex shedding frequencies within the higher-frequency band ($0.152 \leq St_\alpha \leq 0.211$) [Yeh and Taira, 2019].

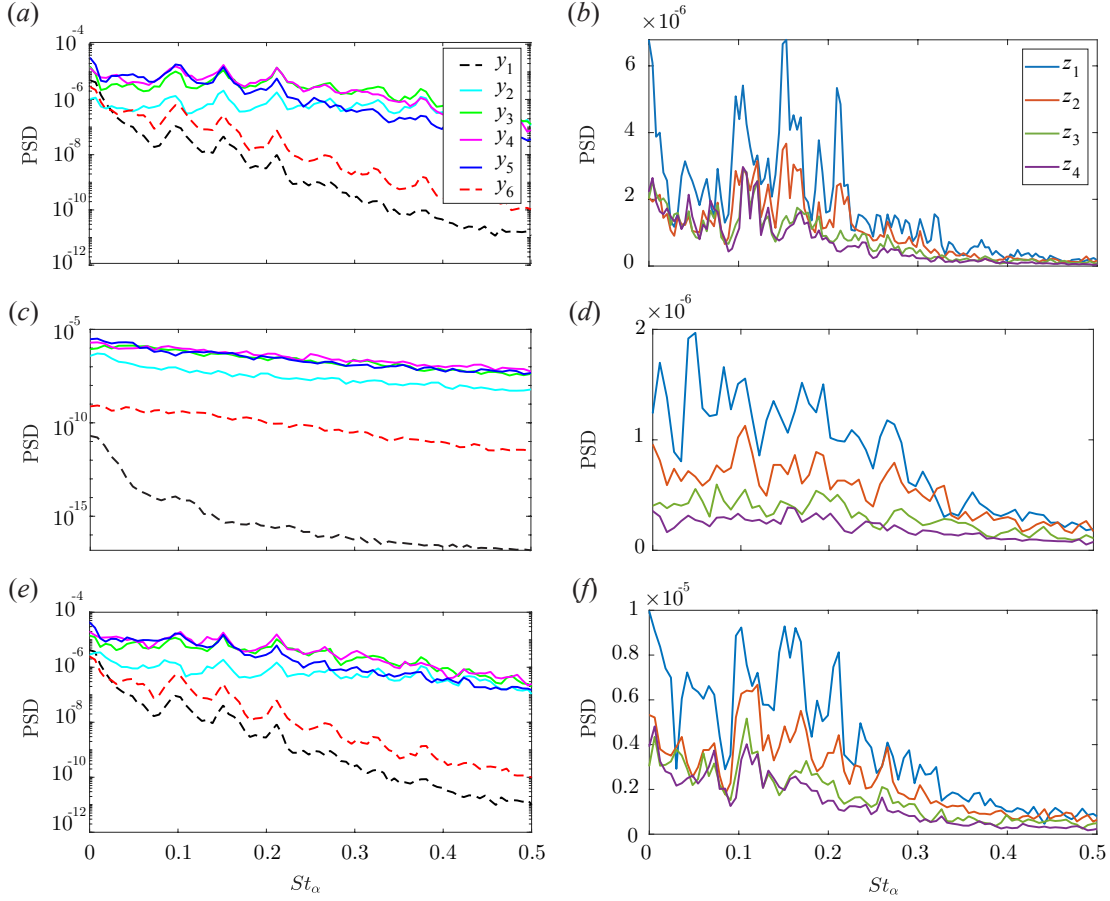


FIGURE 11: PSD of streamwise velocity fluctuations u'_x for sensor readings and target readings, obtained from the spanwise-averaged (a) and (b), spanwise-Fourier ($k_z = 10\pi$) (c) and (d), and mid-span plane (e) and (f) cases presented in figure 6. In (a), the dashed lines indicate positions y_1 and y_6 , corresponding to the laminar flow region.

Figure 11(c) and (d) illustrate the PSD of sensor and target measurements for the spanwise-Fourier mode at the wavenumber $k_z = 10\pi$, respectively. The PSD computations utilize the same parameters as those used for the spanwise-averaged case. Compared to the spanwise-averaged (a) and mid-span plane (e) cases, the PSD at the sensor and target locations (c) does not exhibit distinct dominant peaks, consistent with the coherence results shown in figure 10. As observed in Yeh and Taira [2019] and Towne et al. [2023], the response modes for spanwise-Fourier modes at $k_z = 10\pi$ appear predominantly slightly away from the airfoil surface. Thus, the spanwise Fourier modes at the sensor locations are relatively weak, leading to weaker PSD values, as illustrated in figure 11(c). Modes at lower wavenumbers correspond to larger, more energetic spanwise structures, whereas modes at higher wavenumbers represent smaller, less energetic structures. We confirmed that the primary difference between the wavenumbers $k_z = 10\pi$ and 20π is the magnitude of their PSD values, while their PSD patterns remain similar.

Figure 11(e) and (f) display the PSD of sensor and target signals in the mid-span plane. Similar to the spanwise-averaged case, the laminar flow region (y_1 and y_6) exhibits lower energy fluctuations. Additionally, energy progressively dissipates as the target moves further downstream. Dominant frequencies in the approximate range $0.1 < St_\alpha < 0.2$ are distinctly visible in the near-wake targets (z_1 and z_2), as clearly

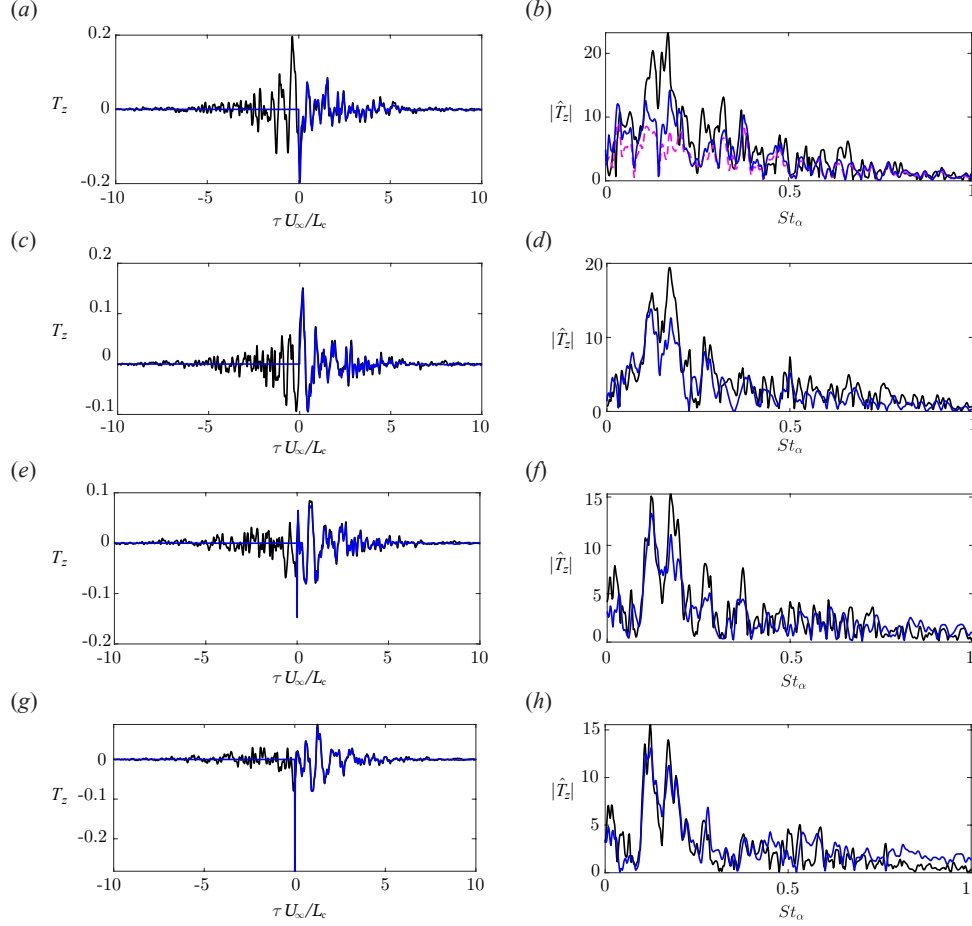


FIGURE 12: Estimation kernels between sensor y_1 and targets z_1 (a, b), z_2 (c, d), z_3 (e, f), and z_4 (g, h) for the spanwise-averaged flow. Kernels are shown in the time domain (left column) and frequency domain (right column). The black line represents the non-causal kernel, the blue line represents the causal kernel obtained via Wiener–Hopf decomposition, and the magenta dashed line (when shown) indicates the truncated non-causal kernel.

illustrated in panel (f).

4.3 Estimation kernels

Next, we examine the estimation kernels, building on our previous studies [Martini et al., 2020, 2022, Jung et al., 2025], where we initially explored kernels within the resolvent-based framework. In this paper, we derive the kernels using a data-driven approach that accounts for the statistical effects of flow nonlinearity, implicitly incorporating the CSD matrix $\hat{\mathbf{F}}_{nl}$, which acts as a forcing in linear dynamics. Note that when white noise forcing is applied, the estimation kernels correspond to the transfer functions of the Kalman filter [Kalman, 1960], as shown by Martini et al. [2022]. Incorporating the forcing matrix $\hat{\mathbf{F}}_{nl}$ is suitable for this study, as our application involves strongly nonlinear turbulent flows. Modeling the nonlinear terms for estimation leads to better performance. A key characteristic of estimation kernels is the presence of peak points, which reveal the time it takes for hydrodynamic waves to travel from the sensor location to the target. Since the estimation kernels are based on the compressible linearized Navier-Stokes operator, they also capture

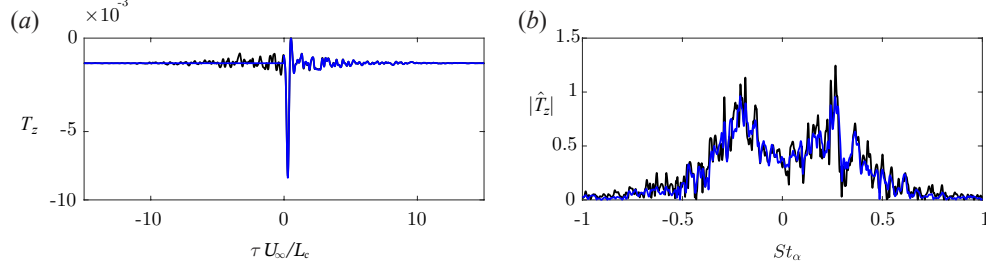


FIGURE 13: Estimation kernels between sensor y_5 and target z_1 for the spanwise Fourier mode at $k_z = 10\pi$, shown in the time (a) and frequency (b) domains. Sensor and target positions are indicated in figure 6. The black line represents the non-causal kernel, and the blue line represents the causal kernel obtained via Wiener–Hopf decomposition.

acoustic waves, resulting in secondary peaks in addition to the hydrodynamic waves [Jung et al., 2023, Towne et al., 2024]. Another important characteristic is whether there are significant values in the non-causal part of the kernel ($\tau < 0$), including the peak point [Jung, 2024]. This information is crucial for estimation, but it may be truncated when the estimator is applied to the convolution function if it resides in the non-causal part of the kernels. This truncation can lead to a significant difference in the performance between the causal and truncated non-causal approaches. From a numerical perspective, the estimation kernels function by amplifying the frequency signals of the sensor measurements through multiplication with the kernels to approximate the target signals, i.e., $\hat{z}(\omega) = \hat{T}_z(\omega)\hat{y}(\omega)$. Therefore, analyzing the estimation kernels in the frequency domain alongside the PSD of the sensor and target readings in §4.2 provides valuable numerical insights into accurate estimation.

We examine four kernels, specifically within the single input and multiple outputs configuration (sensor: y_1 and targets: z_1, z_2, z_3, z_4), as illustrated in figure 12. This selection is based on the observation that when the sensor is positioned in the laminar region within the effective locations, the kernel’s peaks are distinct, with less noise in other frequencies, showing a clear correlation between the sensor and the target signals. In figure 12, prominent peak points are observed in the non-causal kernels (a, c, e, g) at $[\tau_{\text{peak},z_1}, \tau_{\text{peak},z_2}, \tau_{\text{peak},z_3}, \tau_{\text{peak},z_4}] = [-0.360, 0.171, 0.676, 1.25]$, respectively. These points represent the primary hydrodynamic wave travel times between the sensor and the targets. The case in figure 12(a) serves as a good example of how a causal approach using Wiener-Hopf decomposition can enhance estimation accuracy. When this kernel is applied to real-time estimation for evaluating the convolution function, the peak at $\tau = -0.36$, which contains critical travel information of the fluctuations, is truncated. The truncated non-causal kernel in the frequency domain (magenta dashed line) is notably lower in magnitude compared to the causal kernel (blue line), as shown in 12(b). It is important to note that the kernels amplify the sensor measurements at dominant frequencies ($0.1 < St_\alpha < 0.2$).

Imposing sensor is necessary to ensure that the inversion of the PSD is well-posed [Martini et al., 2020, 2022]. The noise level, which is used to regularize the kernels, is set at 10^{-2} of the maximum PSD value of the sensor measurements, consistent with the approach used in previous work [Martini et al., 2022, Jung et al., 2025]. Similar to other optimal estimation and control methods [Chevalier et al., 2006, Schmid and Sipp, 2016], the sensor noise is described by correlations that are assumed to be known.

Figure 13 shows the kernels for the spanwise-Fourier modes at $k_z = 10\pi$. Based on figure 7, sensor placement in the laminar region is less effective; hence, we focus on kernels corresponding to sensor y_5 , rather than y_1 , and target z_1 , consistent with locations examined previously in figure 12. Because the spanwise Fourier-transformed state is complex-valued, the computational cost for estimation increases by a factor of four. Additionally, the kernels are no longer symmetric at $St_\alpha = 0$, as shown in figure 13. The peak

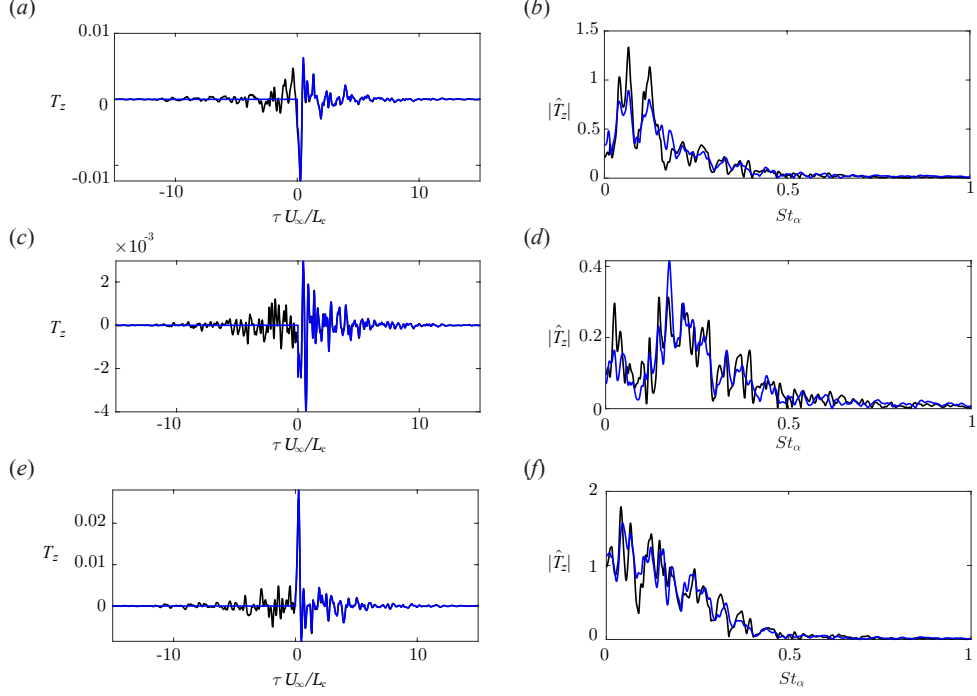


FIGURE 14: Estimation kernels between sensors y_1 (a, b), y_5 (c, d), and y_6 (e, f) and target z_1 for the mid-span plane case. Kernels are shown in the time domain (left column) and frequency domain (right column). The black line represents the non-causal kernel, and the blue line represents the causal kernel obtained via Wiener–Hopf decomposition.

points are clearly visible (see figures 13(a) and (c)) at $\tau > 0$, indicating the dominance of hydrodynamic waves. Consequently, performance differences between causal and truncated non-causal estimation methods are minimal. The values of the kernels are largest in the range of $|St_\alpha| < 0.2$, effectively amplifying sensor measurements to produce accurate estimates.

Finally, we present the kernels for the mid-span plane flow in figure 14. Sensors positioned in both the laminar (y_1) and turbulent regions (suction side: y_5 ; pressure side: y_6) are shown. The prominent peak points in the kernels between sensors (y_1, y_5) and target z_1 closely match those observed in the spanwise-averaged and spanwise-Fourier flows, respectively, as depicted in figures 12 and 13 for the kernels between y_1 and z_1 and y_5 and z_1 , respectively. The kernel between y_6 and z_1 also aligns well with the other cases, though it is not explicitly shown here. However, the kernels for the mid-span flow exhibit significant amplitudes over a larger range of τ , indicating greater difficulty in achieving temporal convergence. A notable difference appears in figure 14(a), where the kernel peak lies in the positive domain ($\tau > 0$), unlike the corresponding kernel in the spanwise-averaged flow, which peaks in the negative domain. This discrepancy may be attributed to the fact that the spanwise-averaged case integrates the flow across multiple spanwise positions, capturing coherent large-scale structures that extend significantly in the spanwise direction. These large-scale structures are more capable of influencing upstream conditions (non-causal behavior), appearing as peaks in the non-causal part ($\tau < 0$) of the kernel. In contrast, the mid-span plane case represents a single spanwise slice, emphasizing smaller-scale, localized spatial structures. Such structures typically have limited upstream influence since their acoustic disturbances are weaker, more rapidly dissipated, and less coherent over larger spanwise distances. Thus, such conditions enhance convective flow characteristics in the mid-span plane case, thereby improving the accuracy when applying truncated non-causal estimation to the mid-span plane

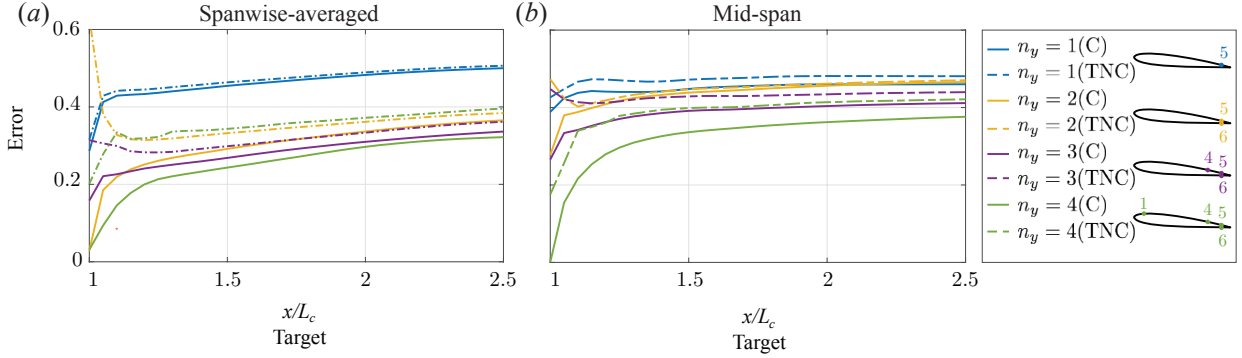


FIGURE 15: Estimation error along the trailing edge for spanwise-averaged and mid-span flows using one sensor (y_5), two sensors (y_5, y_6), three sensors (y_4, y_5, y_6), and four sensors (y_1, y_4, y_5, y_6).

flow. Additionally, we observe that the kernel between y_4 and z_1 is similar to that between y_5 and z_1 within the mid-span flow, so it is omitted from this figure. Both causal and truncated non-causal kernels for targets further downstream (z_2, z_3, z_4) closely resemble those in the spanwise-averaged flow (figure 12), with their peak points consistently located in the positive τ domain.

4.4 Multi-sensor estimation

By selecting sensor locations $y_1, y_4, y_5,$ and y_6 (notations from figure 9(a) and (b)) based on the investigation of the most effective locations using single-sensor estimation and coherence in §4.1, we show the estimation errors for spanwise-averaged and mid-span flows along the trailing edge as additional sensors are introduced, as shown in figure 15. The use of sensor y_5 (blue) alone does not yield significant improvement over truncated non-causal estimation. However, adding an additional sensor (y_6) markedly enhances estimation accuracy (yellow). With these two sensors, truncated non-causal estimation performs poorly near the trailing edge, whereas causal estimation remains accurate. The inclusion of a third sensor y_4 (purple) alongside y_5 and y_6 results in a slight improvement. The best estimation results are achieved using all four sensors y_1, y_4, y_5, y_6 (green). These findings demonstrate greater accuracy than the use of six sensors uniformly distributed on the pressure side of the airfoil, as reported in our previous work [Jung and Towne, 2024].

Figure 16 shows the time-series estimation of streamwise velocity fluctuations using four sensors (y_1, y_4, y_5, y_6) for spanwise-averaged (panels a, d, g, j), mid-span plane (panels b, e, h, k), and spanwise-Fourier (panels c, f, i, l) cases. The causal estimation error, computed using (4.1), is indicated in the bottom right corner of each panel. As expected, the estimation error increases with greater distance between the sensor and the target location. The Wiener–Hopf approach significantly improves estimation accuracy for targets located closer to the trailing edge, as evident in figure 16(a). The difference in accuracy between truncated non-causal (TNC) and causal methods diminishes as the target moves further downstream. Among the investigated flow types, the spanwise-averaged flow, characterized by less chaotic spatial structures, is estimated most accurately. For the mid-span plane flow, presented in figure 16 (panels b, e, h, k), the time-series velocity fluctuations exhibit more random oscillations compared to the other flow types considered. However, despite this increased complexity, the broader trends in the velocity fluctuations over time are still effectively captured. Although the sensor may not fully capture the detailed footprint of turbulence, the estimation remains effective. These results are consistent with the trends shown in figure 15.

Figure 16 (panels c, f, i, l) displays time-series estimations of the real part of u'_x for the spanwise-Fourier

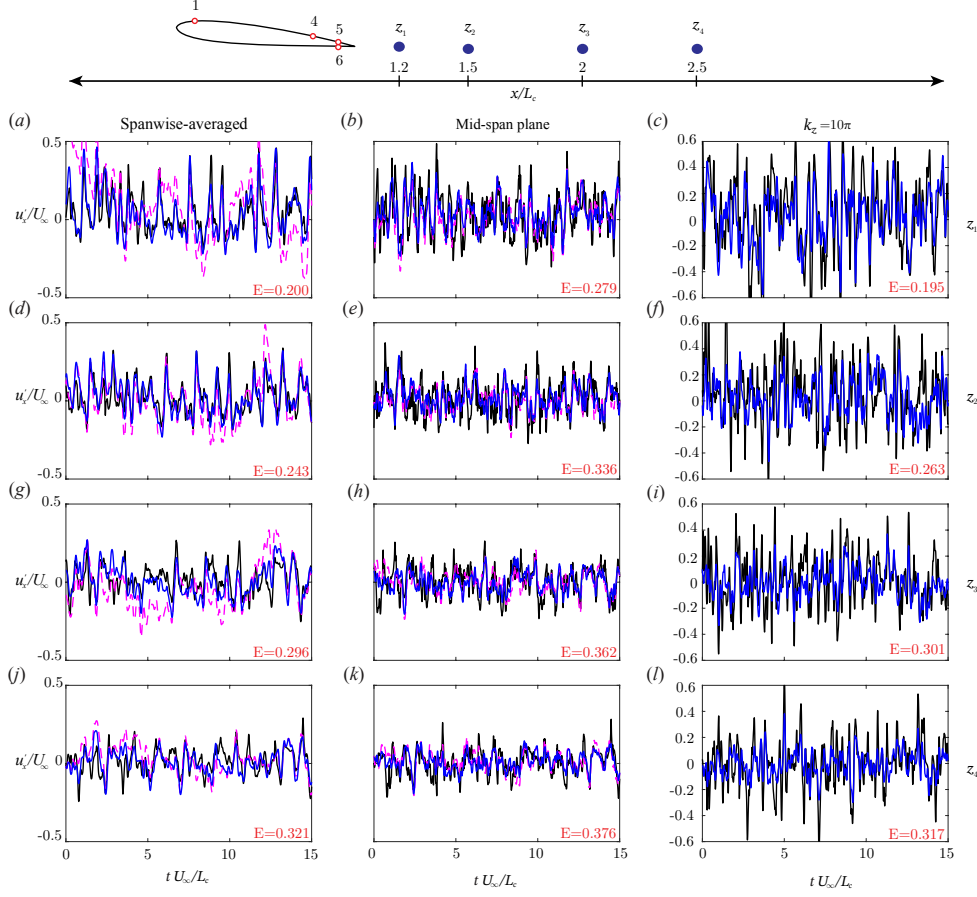


FIGURE 16: Estimation of u'_x as a function of time using four sensors (y_1, y_4, y_5, y_6): spanwise-averaged (panels *a, d, g, j*), mid-span plane (panels *b, e, h, k*), spanwise-Fourier cases at $k_z = 10\pi$ (panels *c, f, i, l*). Target locations are defined by coordinates $[z_1 = x/L_c, y/L_c]$: panels (*a-c*) at $[1.2, -0.11]$, (*d-f*) at $[1.5, -0.11]$, (*g-i*) at $[2.0, -0.11]$, and (*j-l*) at $[2.5, -0.11]$, as illustrated in the top figure. The true data from LES are shown in black, causal estimations in blue, and truncated non-causal estimations as magenta dashed lines. The causal estimation error is indicated in red in the bottom right corner of each panel.

modes with $k_z = 10\pi$. As anticipated, estimation accuracy decreases with increasing spanwise wavenumber. Kernels derived from resolvent operators at frequencies associated with lower energetic gains provide lower estimation accuracy. Since the TNC and causal estimations for the spanwise-Fourier modes yield similar results, the TNC estimations are not shown explicitly in figure 16 for these cases.

Figure 17 shows three random snapshots of the causal estimation in the extended wake region for spanwise-averaged and mid-span plane cases, using the same sensor configuration as in figure 16. The estimation errors for the wake region, calculated using metric 4.1, are approximately 0.254 and 0.324 for causal estimation, and 0.352 and 0.389 for truncated non-causal estimation in the spanwise-averaged and mid-span plane cases, respectively. Although the small-scale structures are not fully captured due to the limitations of the sensors in detecting turbulence, the causal resolvent-based estimator effectively estimates the wake fluctuations. Given that the estimation relies solely on a limited number (four sensors) of real-time measurements, these results demonstrate significant promise for practical applications in experimental settings and other engineering scenarios.

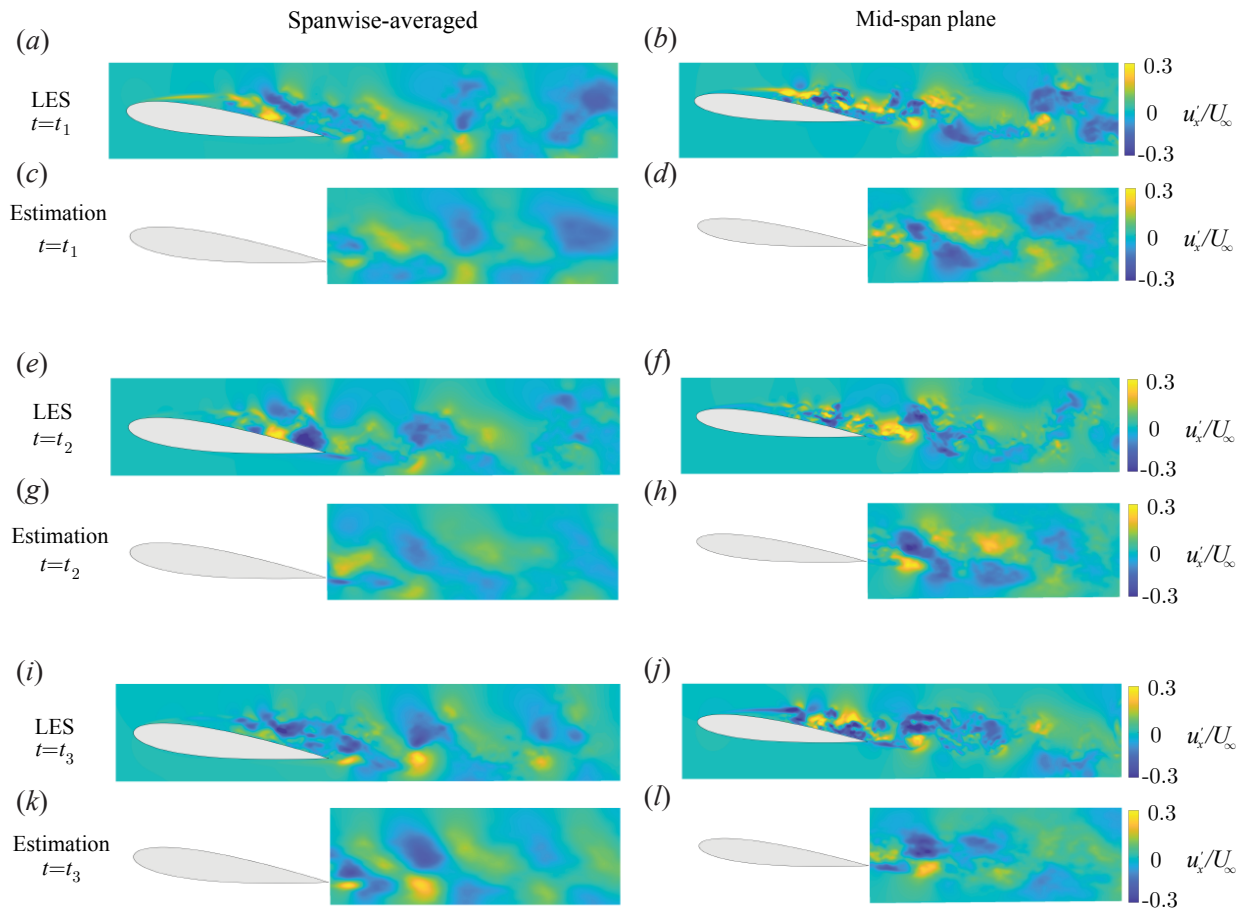


FIGURE 17: LES and estimated snapshots of u'_x across the extended wake region for the spanwise-averaged (panels *a, c, e, g, i, k*) and mid-span plane (panels *b, d, f, h, j, l*) flows, utilizing four sensors (y_1, y_4, y_5, y_6). The times t_1, t_2 , and t_3 were chosen to represent three distinct phases based on the dominant vortex shedding frequency.

5 Conclusions

In this study, we developed and demonstrated a causal resolvent-based framework for estimating turbulent velocity fluctuations in the wake of a spanwise-periodic NACA0012 airfoil at moderate Reynolds $Re_{Lc} = 23,000$, $Ma_\infty \equiv U_\infty/c_\infty = 0.3$, and an angle of attack of $\alpha = 6^\circ$. Building on previous research focused primarily on a laminar and globally stable flow scenario [Jung et al., 2025], our approach extended resolvent-based estimation into the more complex regime of a turbulent, globally unstable wake flow.

To address the key challenges inherent in this turbulent regime, including global instabilities, broadband multiscale dynamics, and large datasets, we employed a data-driven approach. This allowed construction of resolvent-based kernels from cross-spectral densities directly obtained via large-eddy simulations, inherently incorporating the colored-in-time statistical properties of nonlinear forcing terms. A key improvement was the adoption of the Wiener–Hopf method to enforce causality [Martini et al., 2022], which significantly enhanced real-time estimation accuracy compared to traditional truncated, non-causal estimators. To handle computational complexity arising from high-dimensional datasets, our methodology utilized scalable parallel

algorithms integrated within an existing compressible flow solver [Jung et al., 2024, Towne et al., 2024].

Our results illustrated successful causal estimation across spanwise-averaged, spanwise-Fourier, and mid-span plane representations of the turbulent wake, using only limited shear-stress measurements from the airfoil surface. By strategically analyzing single-sensor estimation errors and coherence between sensor and target locations, we identified practical sensor-placement strategies that significantly enhanced estimation fidelity. Ultimately, our approach provided accurate, interpretable, and scalable predictions of an extended portion of the wake, capturing dominant coherent structures crucial for both scientific understanding and potential flow control applications.

Future research directions suggested by this study include developing formal optimization methods for sensor placement and incorporating three-dimensional sensor configurations to further enhance estimation accuracy. The success of the resolvent-based estimation framework suggests that resolvent-based closed-loop flow control strategies could help mitigate turbulent fluctuations, reduce drag, increase lift, and minimize aerodynamic noise. It would also be valuable to investigate the generalizability and robustness of this approach under varying flow conditions, different airfoil geometries, higher Reynolds numbers, and more complex aerodynamic environments. Integrating advanced machine-learning techniques, such as neural networks, into the resolvent-based framework would further improve real-time computational efficiency and effectively handle larger datasets. Finally, experimental validation of the proposed resolvent-based estimation approach in practical wind-tunnel tests or flight scenarios is recommended to confirm its real-world applicability and robustness. By pursuing these avenues, our resolvent-based estimation framework has the potential to significantly advance the predictive modeling, real-time monitoring, and control of complex turbulent aerodynamic flows.

Funding

This research was supported by the Air Force Office of Scientific Research (AFOSR) under grant number FA9550-20-1-0214. Computational resources were provided by the U.S. Department of Defense High-Performance Computing Modernization Program.

Declaration of interests

The authors report no conflict of interest.

Author ORCIDs

 Junoh Jung <https://orcid.org/0000-0003-0962-3127>;

 Aaron Towne <https://orcid.org/0000-0002-7315-5375>.

Appendix A Wiener-Hopf method

We briefly review the theoretical and numerical Wiener–Hopf decompositions employed for enforcing causality within the resolvent-based estimation and control framework described by Martini et al. [2022], Audiffred et al. [2023], Jung et al. [2025].

A.1 Theoretical Wiener-Hopf decomposition

The Wiener-Hopf method [Noble, 1958] decomposes frequency-domain functions into causal (analytic in lower half-plane, (+)) and non-causal (analytic in upper half-plane, (–)) components. This decomposition

is employed here to enforce causality on estimation and control kernels, following [Daniele and Lombardi \[2007\]](#), [Martinelli \[2009\]](#).

We consider the Wiener-Hopf problem

$$\hat{\mathbf{H}}(\omega)\hat{\mathbf{F}}_+(\omega) = \hat{\boldsymbol{\Lambda}}_-(\omega) + \hat{\mathbf{G}}(\omega), \quad (\text{A.1})$$

where $\hat{\mathbf{H}}$ and $\hat{\mathbf{G}}$ are known matrices, while $\hat{\mathbf{F}}_+$ and $\hat{\boldsymbol{\Lambda}}_-$ are unknown.

The Wiener-Hopf method involves additive and multiplicative factorizations, defined as

$$\hat{\mathbf{F}}(\omega) = [\hat{\mathbf{F}}(\omega)]_- + [\hat{\mathbf{F}}(\omega)]_+, \quad \hat{\mathbf{F}}(\omega) = (\hat{\mathbf{F}}(\omega))_- (\hat{\mathbf{F}}(\omega))_+, \quad (\text{A.2})$$

respectively. The explicit solution for the above problem is

$$\hat{\mathbf{F}}_+(\omega) = \left[\hat{\mathbf{G}}(\omega) (\hat{\mathbf{H}}(\omega))_-^{-1} \right]_+ (\hat{\mathbf{H}}(\omega))_+^{-1}. \quad (\text{A.3})$$

A.2 Numerical Wiener-Hopf decomposition

Numerically, the additive factorization is straightforward, while the multiplicative factorization requires solving an integral equation. Following [Martini et al. \[2022\]](#), this integral equation is given by

$$\hat{\mathbf{x}}_i(\omega) + \frac{1}{2i} \mathcal{H}(\hat{\mathbf{x}}_i)(\omega) - \frac{1}{2i} \hat{\mathbf{G}}^{-1}(\omega) \mathcal{H}(\hat{\mathbf{G}}\hat{\mathbf{x}}_i)(\omega) = \hat{\mathbf{G}}^{-1}(\omega) \frac{\hat{\mathbf{w}}_{i,-}(\omega_0)}{\omega - \omega_0}, \quad (\text{A.4})$$

where \mathcal{H} denotes the Hilbert transform defined by

$$\mathcal{H}(\hat{\mathbf{x}}) = P.V. \frac{1}{\pi} \int_{-\infty}^{\infty} \frac{\hat{\mathbf{x}}(u)}{\omega - u} du. \quad (\text{A.5})$$

The reader is referred to [Noble \[1958\]](#), [Daniele and Lombardi \[2007\]](#), [Martinelli \[2009\]](#), [Martini et al. \[2022\]](#) for a detailed discussion of the Wiener-Hopf method. We numerically solve this integral equation using the GMRES iterative method, implemented directly within the CFD solver. This approach ensures computational efficiency and minimizes the need for external post-processing [\[Jung et al., 2025\]](#).

Appendix B Convergence of the data-driven estimation kernels

Case	N_{freq}	N_{ovlp}	N_{blks}	Error
1	500	250	296	0.400748
2	1,000	500	148	0.350644
3	2,000	1,000	74	0.330292
4	3,000	1,500	48	0.320681
5	4,000	2,000	37	0.320541
6	5,000	2,500	29	0.320422

TABLE 2: Convergence of the estimation kernels with respect to the parameters for the discrete Fourier Transforms used to compute CSDs.

Constructing estimation kernels using a data-driven approach requires careful selection of discrete Fourier transform (DFT) parameters. Specifically, the streaming Fourier transform [\[Schmidt and Towne, 2019\]](#) depends on several key parameters, including the number of frequencies (N_{freq}), the number of data blocks (N_{blk}), and the number of overlapping windows (N_{ovlp}). To reduce spectral leakage between blocks

(N_{blk}), we apply a Hamming window with an overlap of 50% [Trethewey, 2000]. Table 2 summarizes a convergence study evaluating how these parameters influence estimation accuracy within the spanwise-averaged flow under best sensor placement conditions. Based on this analysis, parameter set 6 was selected, and these DFT parameters were subsequently applied to the spanwise-Fourier and mid-span plane cases examined in this study.

References

- F. R. Amaral and A. V. G. Cavalieri. Large-eddy-simulation-informed resolvent-based estimation of turbulent pipe flow. *Phys. Rev. Fluids*, 8(7):074606, July 2023. ISSN 2469-990X. doi: 10.1103/PhysRevFluids.8.074606.
- F. R. Amaral, A. V. G. Cavalieri, E. Martini, P. Jordan, and A. Towne. Resolvent-based estimation of turbulent channel flow using wall measurements. *J. Fluid Mech.*, 927:A17, November 2021.
- D. B. S. Audiffred, A. V. G. Cavalieri, P. P. C. Brito, and E. Martini. Experimental control of Tollmien-Schlichting waves using the Wiener-Hopf formalism. *Phys. Rev. Fluids*, 8(7):073902, July 2023.
- D. B. S. Audiffred, A. V. G. Cavalieri, I. A. Maia, E. Martini, and P. Jordan. Reactive experimental control of turbulent jets. *J. Fluid Mech.*, 994:A15, September 2024. ISSN 0022-1120, 1469-7645. doi: 10.1017/jfm.2024.569.
- S. Balay, S. Abhyankar, M. Adams, and Others. Petsc users manual. *Argonne National Laboratory*, 2019.
- R. Bhagwat. Development of stability analysis tools for high speed compressible flows. *PhD thesis*, 2021.
- G. A. Brès, S. T. Bose, C. B. Ivey, M. Emory, and F. Ham. Gpu-accelerated large-eddy simulations of supersonic jets from twin rectangular nozzles. *AIAA Paper #2022-3001*, 2022.
- G. A. Brès, F. E. Ham, J. W. Nichols, and S. K. Lele. Unstructured large-eddy simulations of supersonic jets. *AIAA J.*, 2017.
- G. A. Brès, P. Jordan, V. Jaunet, M. Le Rallic, A. V. G. Cavalieri, A. Towne, S. K. Lele, T. Colonius, and O. T. Schmidt. Importance of the nozzle-exit boundary-layer state in subsonic turbulent jets. *J. Fluid Mech.*, 851:83–124, September 2018. ISSN 0022-1120, 1469-7645. doi: 10.1017/jfm.2018.476.
- M. Chevalier, J. Hœpffner, T. R. Bewley, and D. S. Henningson. State estimation in wall-bounded flow systems. Part 2. Turbulent flows. *J. Fluid Mech.*, 552(-1):167, March 2006. ISSN 0022-1120, 1469-7645. doi: 10.1017/S0022112005008578.
- T. Colonius and A. Towne. Chapter 2 - Modal decomposition. In Karthik Duraisamy, editor, *Computation and Analysis of Turbulent Flows*, pages 27–81. Academic Press, 2025. ISBN 978-0-323-95043-5. doi: <https://doi.org/10.1016/B978-0-32-395043-5.00008-5>.
- V. Daniele and G. Lombardi. Fredholm factorization of Wiener-Hopf scalar and matrix kernels. *Radio Science*, 42(6):2007RS003673, December 2007.
- A. Ducoin, J.-Ch. Loiseau, and J.-Ch. Robinet. Numerical investigation of the interaction between laminar to turbulent transition and the wake of an airfoil. *European J. Mech. - B/Fluids*, 57:231–248, May 2016. ISSN 09977546. doi: 10.1016/j.euromechflu.2016.01.005.
- A. Farghadan, J. Jung, R. Bhagwat, and A. Towne. Efficient harmonic resolvent analysis via time stepping. *Theor. Comput. Fluid Dyn.*, May 2024. ISSN 0935-4964, 1432-2250. doi: 10.1007/s00162-024-00694-1.
- A. Farghadan, E. Martini, and A. Towne. Scalable resolvent analysis for three-dimensional flows. *J. Comput. Phys.*, 524:113695, March 2025. ISSN 00219991. doi: 10.1016/j.jcp.2024.113695.
- P. F. Fischer, J. W. Lottes, and S. G. Kerkemeier. Nek5000: Open source spectral element cfd solver, 2008.
- M. Frigo and S.G. Johnson. The Design and Implementation of FFTW3. *Proc. IEEE*, 93(2):216–231, February 2005.

- I. S. Gartshore. Two-dimensional turbulent wakes. *J. Fluid Mech.*, 30(3):547–560, November 1967. ISSN 0022-1120, 1469-7645. doi: 10.1017/S0022112067001600.
- S. Ghaemi and F. Scarano. Counter-hairpin vortices in the turbulent wake of a sharp trailing edge. *J. Fluid Mech.*, 689:317–356, December 2011. ISSN 0022-1120, 1469-7645. doi: 10.1017/jfm.2011.431.
- S. Gupta, J. Zhao, A. Sharma, A. Agrawal, K. Hourigan, and M. C. Thompson. Two- and three-dimensional wake transitions of a NACA0012 airfoil. *J. Fluid Mech.*, 954:A26, January 2023. ISSN 0022-1120, 1469-7645. doi: 10.1017/jfm.2022.958.
- R. W. Hamming. *Digital filters*. Dover Publications, 1997.
- M. Hočevár, B. Širok, and I. Grabec. A Turbulent-Wake Estimation Using Radial Basis Function Neural Networks. *Flow Turbul. Combust.*, 74(3):291–308, April 2005. ISSN 1386-6184, 1573-1987. doi: 10.1007/s10494-005-5728-4.
- B. Jin, S. J. Illingworth, and R. D. Sandberg. Optimal sensor and actuator placement for feedback control of vortex shedding. *J. Fluid Mech.*, 932:A2, February 2022.
- M. R. Jovanović and B. Bamieh. Componentwise energy amplification in channel flows. *J. Fluid Mech.*, 534:145–183, June 2005.
- J. Jung. Resolvent-based estimation and control of aerodynamic flows. *PhD thesis*, 2024.
- J. Jung and A. Towne. Toward turbulent wake estimation using a resolvent-based approach. *AIAA Paper #2024-0057*, 2024.
- J. Jung, E. Martini, A. Cavalieri, P. Jordan, L. Lesshafft, and A. Towne. Optimal resolvent-based estimation for flow control. *APS Division of Fluid Dynamics*, G06:004, 2020.
- J. Jung, R. Bhagwat, and A. Towne. Resolvent-based estimation of laminar flow around an airfoil. *AIAA Paper #2023-0077*, 2023.
- J. Jung, R. Bhagwat, and A. Towne. Resolvent-based estimation and control of a laminar airfoil wake, December 2024. arXiv:2412.19386.
- J. Jung, R. Bhagwat, and A. Towne. Resolvent-based estimation and control of a laminar airfoil wake. *J. Fluid Mech.*, 0, 2025. doi: 10.1017/jfm.2025.10423.
- R.E. Kalman. A new approach to linear filtering and prediction problems. *J. Basic Engng*, 82:35–45, 1960.
- D.-H. Kim, J.-H. Yang, J.-W. Chang, and J. Chung. Boundary layer and near-wake measurements of naca 0012 airfoil at low reynolds numbers. *AIAA Paper #2009-1472*, 2009.
- R. Kojima, T. Nonomura, A. Oyama, and K. Fujii. Large-Eddy Simulation of Low-Reynolds-Number Flow Over Thick and Thin NACA Airfoils. *J. Aircraft*, 50(1):187–196, 2013.
- Q. Liu, Y. Sun, C. Yeh, L. S. Ukeiley, L. N. Cattafesta, and K. Taira. Unsteady control of supersonic turbulent cavity flow based on resolvent analysis. *J. Fluid Mech.*, 925:A5, October 2021. ISSN 0022-1120, 1469-7645.
- I. A. Maia, P. Jordan, A. V. G. Cavalieri, E. Martini, K. Sasaki, and F. J. Silvestre. Real-time reactive control of stochastic disturbances in forced turbulent jets. *Phys. Rev. Fluids*, 6(12):123901, December 2021. ISSN 2469-990X. doi: 10.1103/PhysRevFluids.6.123901.
- K. Manohar, B. W. Brunton, J. N. Kutz, and Brunton S. L. Data-Driven Sparse Sensor Placement for Reconstruction: Demonstrating the Benefits of Exploiting Known Patterns. *IEEE Control Syst.*, 38(3): 63–86, June 2018. ISSN 1066-033X, 1941-000X. doi: 10.1109/MCS.2018.2810460.
- F. Martinelli. Feedback Control of Turbulent Wall Flows. *PhD thesis*, 2009.
- E. Martini, A. V. G. Cavalieri, P. Jordan, A. Towne, and L. Lesshafft. Resolvent-based optimal estimation of transitional and turbulent flows. *J. Fluid Mech.*, 900:A2, October 2020. ISSN 0022-1120, 1469-7645.

- E. Martini, J. Jung, A. Cavalieri, P. Jordan, and A. Towne. Resolvent-based tools for optimal estimation and control via the Wiener–Hopf formalism. *J. Fluid Mech.*, 937:A19, April 2022.
- B. J. McKeon and A. S. Sharma. A critical-layer framework for turbulent pipe flow. *J. Fluid Mech.*, 658:336–382, September 2010.
- P. M. Munday and K. Taira. Effects of wall-normal and angular momentum injections in airfoil separation control. *AIAA J.*, 2018.
- E. J. Nielsen and W. L. Kleb. Efficient construction of discrete adjoint operators on unstructured grids using complex variables. *AIAA J.*, 2006.
- B. Noble. *Methods Based on the Wiener-Hopf Technique for the Solution of Partial Differential Equations*, volume 7 of *Int. Ser. Monogr. Pure Appl. Math.* Pergamon Press, New York, 1958.
- W. C. Reynolds. Large-scale instabilities of turbulent wakes. *J. Fluid Mech.*, 54(3):481–488, August 1972. ISSN 0022-1120, 1469-7645. doi: 10.1017/S0022112072000813.
- P. Sashittal and D. J. Bodony. Data-driven sensor placement for fluid flows. *AIAA Paper #2021-2824*, 2021.
- C. J. Schauerte and A. Schreyer. Experimental investigation on the turbulent wake flow in fully established transonic buffet conditions. *CEAS Aeronautical J.*, 15(1):125–147, January 2024. ISSN 1869-5582, 1869-5590. doi: 10.1007/s13272-023-00690-x.
- P. J. Schmid and D. Sipp. Linear control of oscillator and amplifier flows. *Phys. Fluids*, 1(4):040501, August 2016. ISSN 2469-990X.
- O. T. Schmidt and A. Towne. An efficient streaming algorithm for spectral proper orthogonal decomposition. *Comput. Phys. Communi.*, 237:98–109, April 2019. ISSN 00104655. doi: 10.1016/j.cpc.2018.11.009.
- S. Shamsoddin and F. Porté-Agel. Turbulent planar wakes under pressure gradient conditions. *J. Fluid Mech.*, 830:R4, November 2017. ISSN 0022-1120, 1469-7645. doi: 10.1017/jfm.2017.649.
- V. Theofilis. Advances in global linear instability analysis of nonparallel and three-dimensional flows. *Prog. in Aerosp. Sci.*, 39(4):249–315, May 2003. ISSN 03760421. doi: 10.1016/S0376-0421(02)00030-1.
- A. Towne, O. T. Schmidt, and T. Colonius. Spectral proper orthogonal decomposition and its relationship to dynamic mode decomposition and resolvent analysis. *J. Fluid Mech.*, 847:821–867, July 2018.
- A. Towne, A. Lozano-Durán, and X. Yang. Resolvent-based estimation of space–time flow statistics. *J. Fluid Mech.*, 883:A17, January 2020. ISSN 0022-1120, 1469-7645.
- A. Towne, S. T. M. Dawson, G. A. Brès, A. Lozano-Durán, T. Saxton-Fox, A. Parthasarathy, A. R. Jones, H. Biler, C. Yeh, H. D. Patel, and K. Taira. A database for reduced-complexity modeling of fluid flows. *AIAA J.*, 2023.
- A. Towne, R. Bhagwat, Y. Zhou, J. Jung, E. Martini, P. Jordan, D. Audiffred, I. Maia, and A. Cavalieri. Resolvent-based estimation of wavepackets in turbulent jets. *AIAA Paper #2024-3413*, 2024.
- M.W. Trethewey. Window and overlap processing effects on power estimates from spectra. *Mech. Syst. Signal Process.*, 14(2):267–278, March 2000. ISSN 0888-3270. doi: 10.1006/mssp.1999.1274. Publisher: Elsevier BV.
- C. Yeh and K. Taira. Resolvent-analysis-based design of airfoil separation control. *J. Fluid Mech.*, 867:572–610, May 2019. ISSN 0022-1120, 1469-7645.
- C. Yeh, S. I. Benton, K. Taira, and D. J. Garmann. Resolvent analysis of an airfoil laminar separation bubble at $Re = 500\,000$. *Phys. Rev. Fluids*, 5(8):083906, August 2020. ISSN 2469-990X.
- A. Ying, T. Liang, Z. Li, and L. Fu. A resolvent-based prediction framework for incompressible turbulent channel flow with limited measurements. *J. Fluid Mech.*, 976:A31, December 2023. ISSN 0022-1120, 1469-7645. doi: 10.1017/jfm.2023.867.